Remote Sensing Applications: Society and Environment 42 (2026) 101966

Contents lists available at ScienceDirect

Remote Sensing Applications: Society and Environment

journal homepage: www.elsevier.com/locate/rsase

Indirect monitoring of heterogeneous tropical agroforestry systems using active and passive remote sensing

Teiser Sánchez-Fuentes, Darwin Gómez-Fernández *, Jorge A. Fernandez-Jibaja, Jhon F. Oblitas-Troyes, Beimer Chuquibala-Checan, Josué Tafur-Culqui, Rosalia Quichua-Baldeon, Victor H. Taboada-Mitma, Daniel Tineo, Malluri Goñas, Nilton Atalaya-Marin

Centro Experimental Yanayacu, Dirección de Servicios Estratégicos Agrarios (DSEA), Instituto Nacional de Innovación Agraria (INIA), Carretera Jaén San Ignacio KM 23.7, Jaén, Cajamarca, 06801, Peru

A R T I C L E I N F O

Keywords:
LiDAR
Multispectral
Mapping
Canopy
Terra

A B S T R A C T

Monitoring agroforestry systems remains challenging due to canopy heterogeneity and the coexistence of species with contrasting dynamics. While field-based methods offer high accuracy, they are inefficient for rapid and multitemporal structural assessments. This study integrated LiDAR and multispectral data collected using a Matrice 350 RTK equipped with a Zenmuse L2 sensor and a RedEdge-P camera. Raw LiDAR data were processed in DJI Terra v4.1 and subsequently pre-processed and corrected in TerraSolid v23.011, whereas multispectral products were generated in Agisoft Metashape Professional v2.2.1. The derived metrics indicated greater growth in System A, driven by fast-growing species, whereas System B showed an overall reduction with slight increases in the upper percentiles. In addition, MSAVI and MTVI2 were sensitive to canopy structure, while GNDVI and NDRE responded to foliage content. The agreement analysis revealed a slight bias (0.09 m) toward height overestimation by LiDAR compared to the hypsometer, with no apparent proportional error. This approach provides a replicable framework for multitemporal monitoring of structural and physiological changes in tropical vegetation, with potential for regional scaling and application in sustainable forest system management.

1. Introduction

Between 1990 and 2020, approximately 178 million hectares of forest were lost globally, although the annual net loss decreased from 7.8 to 4.7 million hectares (Fao, 2020). This reduction is partly due to the establishment of new forests through natural expansion or reforestation initiatives. However, the net loss remains significant, reflecting an imbalance between deforestation and forest recovery. In the regional context, Peru lost around 3.4 million hectares of forest from 2000 to 2020, primarily in the non-flooded tropical rainforest, with impacts even within protected areas (Móstiga et al., 2024).

These ecosystems provide a wide range of ecosystem services, including climate regulation, food and raw material provision, air and water purification, and erosion control (Brockerhoff et al., 2017). Forests also serve as carbon sinks, mitigating climate change by absorbing large volumes of atmospheric carbon dioxide. Therefore, maintaining their ecological integrity is essential to preserve the

* Corresponding author. Jaén, 06801, Cajamarca, Peru.
E-mail address: darwin.agroresearch@gmail.com (D. Gómez-Fernández).

https://doi.org/10.1016/j.rsase.2026.101966
Received 29 December 2025; Received in revised form 25 February 2026; Accepted 10 March 2026
Available online 11 March 2026

environmental functions that support life on Earth and to ensure the adaptive capacity of human communities in the face of ongoing ecological crises (Anandita et al., 2024; De Benedicto et al., 2025).

Nevertheless, deforestation and climate change have triggered an environmental crisis that severely threatens the planet's health (Sengupta, 2024), degrading ecosystems and disrupting natural balances (dos Reis et al., 2021). Additionally, pests and diseases—favoured by rising temperatures and shifting precipitation patterns—are affecting key forest species (Warlo and Kautz, 2024; Zhao et al., 2023), thereby weakening forest resilience and increasing vulnerability to further disturbances (Prevedello et al., 2019).

In response to these challenges, advanced remote sensing technologies have become essential tools for acquiring high-resolution spatial, spectral, and structural information. Both passive (multispectral) and active (LiDAR) systems are increasingly used (Gu et al., 2020; Santoro et al., 2020; Takhtkeshha et al., 2024), offering a robust foundation for natural resource management, environmental monitoring, and the analysis of complex territorial dynamics.

Monitoring vegetation growth and health in forest systems is key for ecosystem conservation, land-use planning, and sustainable resource management (da Silva et al., 2024; Dash et al., 2018). These technologies have improved the efficiency and accuracy of ecosystem assessments (Dash et al., 2018; Yoshii et al., 2022), allowing for large-scale data collection without direct interventions that could negatively affect the environment (Rejeb et al., 2022).

Remote sensing involves the collection and processing of surface information from platforms that are not in direct contact with the observed object (Calders et al., 2020; Toth and Jóźków, 2016). Technological advances, such as Remotely Piloted Aircraft Systems (RPAS), have expanded the application of remote sensing in forest environments, enabling the monitoring of forest growth and health (Eugenio et al., 2020). RPAS equipped with diverse sensors provide accurate data on composition, structure, biomass, and health—factors of both environmental and economic importance (da Silva et al., 2024; Ecke et al., 2022).

LiDAR sensors integrated into RPAS offer a valuable tool for forest analysis, generating high-resolution, three-dimensional point clouds with great precision (Luo et al., 2023). This technology enables the accurate estimation of key variables such as tree height, canopy roughness, and terrain topography, even in densely vegetated areas (Hyde et al., 2006). By producing digital surface models (DSM) and digital terrain models (DTM), LiDAR supports detailed structural characterization of forest ecosystems across different successional stages (Maguya et al., 2014; Takhtkeshha et al., 2024).

On the other hand, multispectral sensors mounted on RPAS collect reflectance data in specific bands of the electromagnetic spectrum, providing insights into the physiological and biophysical state of vegetation (Tan et al., 2025). These data are used to calculate a range of spectral indices widely applied for assessing vegetation vigour and detecting phenological changes (Avtar et al., 2020; Dash et al., 2018; Stone and Mohammed, 2017). Consequently, they are key tools for monitoring vegetation health and detecting

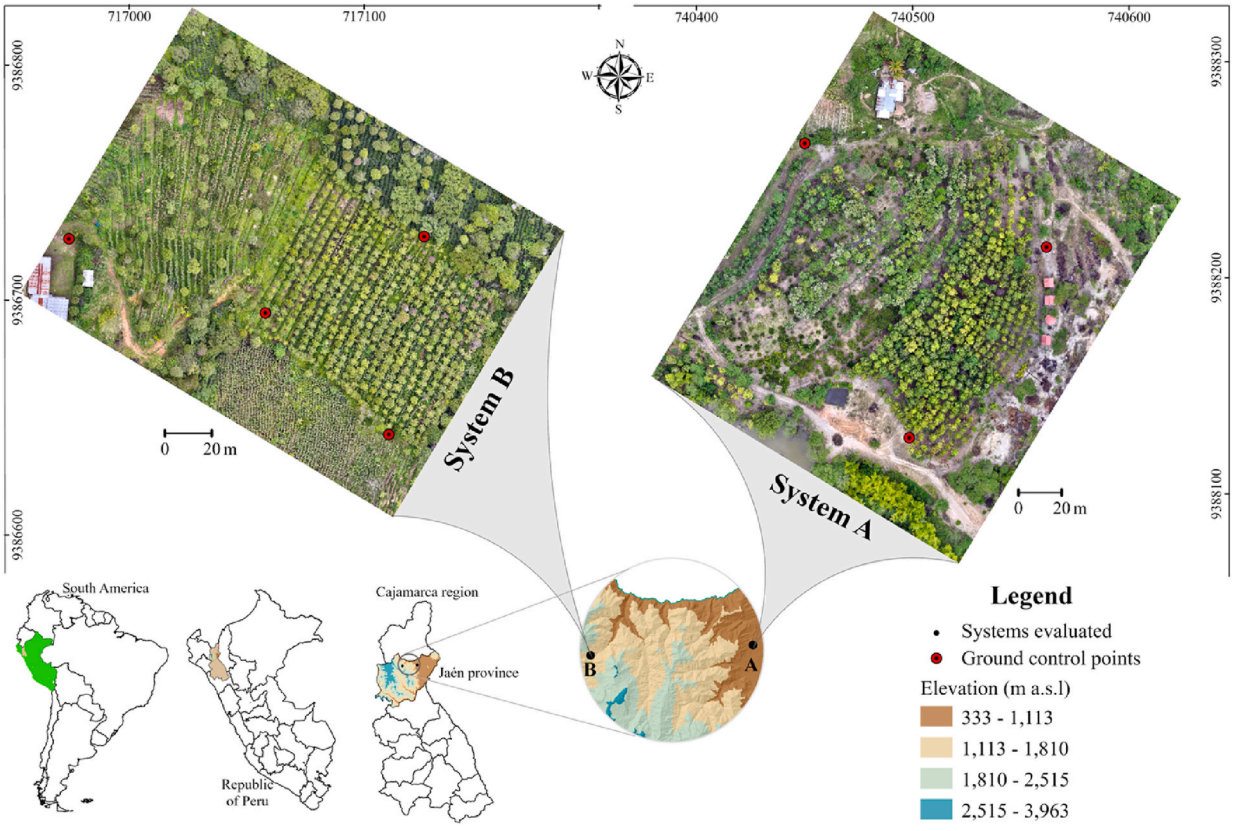

Fig. 1. Location of the evaluated systems in the province of Jaén, Cajamarca region, Peru, South America.

early-stage anomalies.

However, consistent monitoring of forest growth and vegetation health in tropical ecosystems remains a technical and logistical challenge (Yip et al., 2024). Although field-based methods offer local-scale accuracy, they are inefficient for monitoring large forest areas due to high time, labour, and cost requirements. Systematic data collection is also constrained by the inaccessibility of many tropical regions and unfavourable climatic conditions (Dixit et al., 2024). These limitations reduce both the frequency and spatial coverage of monitoring efforts, impairing early detection of degradation or pest outbreaks. The situation is further exacerbated by the lack of infrastructure in remote areas and the reliance on specialized personnel and equipment.

On the other hand, the broader operational adoption of UAV-based LiDAR and multispectral technologies is constrained by high acquisition costs, the need for specialized sensors, software, and trained personnel, and the computational demands of data processing workflows (Fassnacht et al., 2024). These challenges highlight the need to rethink current monitoring approaches, especially in agroforestry systems (AFS), which are increasingly recognized as sustainable land-use strategies in tropical regions but are also characterized by multistate canopies, mixed species composition, and heterogeneous management conditions that complicate monitoring and interpretation (Santoro et al., 2020).

In this context, the present study evaluates the feasibility of an integrated UAV-based LiDAR and multispectral workflow for multitemporal monitoring of heterogeneous tropical vegetation under agroforestry conditions. The study focuses on deriving and validating remote-sensing-based proxies of canopy structure and vegetation condition in a context characterized by canopy

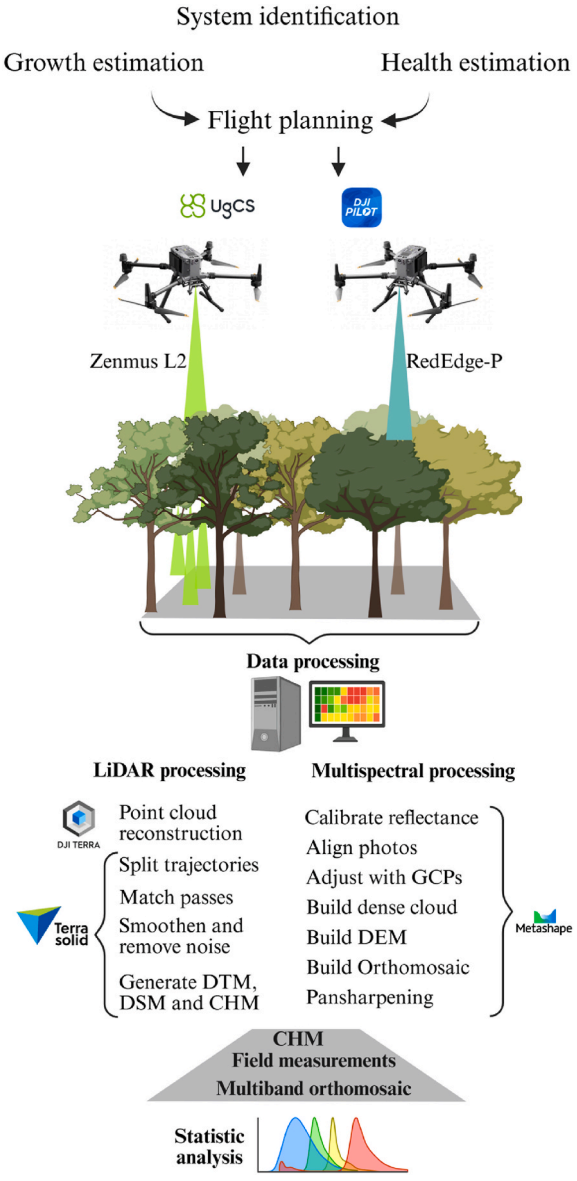

Fig. 2. Methodological workflow used in this study.

heterogeneity and coexisting species with contrasting architectures. To this end, LiDAR and multispectral data were collected at two time points separated by a four-month interval. Structural metrics were derived from LiDAR products, including the validation of height estimates against direct field measurements using a hypsometer. In parallel, several spectral indices relevant to canopy characterization were calculated, and the final set of informative indices was prioritized using principal component analysis. By assessing these indicators across contrasting vegetation scenarios, the study provides an operational and transferable workflow for canopy-level monitoring in complex tropical systems, while acknowledging that broader generalization requires testing in additional sites and species compositions.

2. Materials and methods

2.1. Study area

The study area included two distinct vegetation systems. System A located at an average elevation of 753 m a.s.l. and was primarily composed of eucalyptus (*Eucalyptus saligna*) and capirona (*Calycophyllum spruceanum*). In contrast, System B, located at an average elevation of 1578 m a.s.l., consisted of an agroforestry association of romerillo (*Retrophyllum rospigliosii*) and coffee (*Coffea arabica*). Fig. 1 shows the geographic location of both systems within the Jaén province, Cajamarca region, Peru, South America. System A is characterized by Fluvisol–Phaeozem soils of fluvio-alluvial origin, with gently sloping terrain. According to the Werren Thornthwaite classification, System A corresponds to climate type $C_{(o,i,p)}$A'H3, associated with a semi-dry zone, warm with rainfall deficit and high relative humidity. In contrast, System B is characterized by Andosol–Regosol soils associated with extrusive mountainous formations and steep terrain surfaces. Under the same climatic classification, System B corresponds to climate type $B_{(i)}$B'2H3, representing a temperate rainy zone with winter rainfall deficit and high relative humidity (Gobierno Regional de Cajamarca (GRC), 2010; SENAMHI, 2020).

2.2. Methodological framework

Fig. 2 summarizes the workflow followed to evaluate vegetation growth and canopy health over a four-month period. A monitoring strategy based on remote sensing and field measurements was implemented. Flights were planned using UgCS v5.9.0 and DJI Pilot 2 software. The primary aircraft used was a DJI Matrice 350 RTK equipped with a DJI Zenmuse L2 LiDAR sensor and a MicaSense RedEdge-P multispectral camera. Independent missions were conducted for each sensor to ensure adequate coverage of both the forest canopy and the associated crops.

Subsequently, the collected data were processed through specific workflows. LiDAR data were processed using DJI Terra v4.5.0 and further refined using TerraSolid Suite v23.011 within MicroStation v24.00.002.62 to obtain the products required for analysis. Meanwhile, multispectral images were processed in Agisoft Metashape Professional v2.2.1 for the generation of multiband orthomosaics.

2.2.1. Monitoring design in the evaluated systems

Systems A and B were selected based on criteria of accessibility and contrasting structural composition, aiming to evaluate the ability of active and passive remote sensing to monitor the growth and health of the installed vegetation in each system. A multitemporal monitoring approach was adopted, with flights conducted on March 4 and July 9, 2025, under stable atmospheric conditions to ensure data quality and comparability.

2.2.2. Data acquisition

To monitor vegetation growth, the active sensor DJI Zenmuse L2 was mounted on a DJI Matrice 350 RTK UAV to collect three-dimensional data of the forest canopy structure. Flights were planned using UgCS v5.9.0 under a double-coverage pattern, with sensor inclination angles of 90° and 45°, a flight altitude of 50 m with terrain following, and a LiDAR overlap of 70%. The RGB images captured by the sensor were used to colorize the point cloud, with both forward and side overlaps of 75% during image acquisition. The mission was conducted in RTK flight mode, ensuring centimeter-level positional accuracy, and included the corresponding sensor calibration routines before and during each flight.

To assess vegetation health, the passive MicaSense RedEdge-P multispectral sensor was also mounted on the DJI Matrice 350 RTK, but operated in an independent mission. Flight planning was performed in DJI Pilot 2, maintaining a flight altitude of 50 m with terrain following, 80% forward and 75% side overlaps, and enabling automatic image capture. This sensor recorded reflectance in five spectral bands in the visible and near-infrared range, and included a panchromatic band to generate high-resolution outputs.

Finally, as a field verification measure, manual tree height measurements were conducted during both monitoring periods to validate the results obtained through remote sensing.

2.3. Data processing

2.3.1. Processing of active sensor data

Point cloud reconstruction was carried out in DJI Terra v4.5.0 by importing the LiDAR system files along with the RGB images, as well as four ground control points (GCPs) in System A and three in System B. The processing was performed in high-density mode, using the UTM Zone 17S coordinate system (EPSG:32717) and the EGM2008 geoid as the vertical elevation model. A cell size of 10 cm

was defined, and interpolation was enabled to refine spatial continuity among points.

The resulting point cloud, exported in LAS 1.2 format, was further processed using TerraSolid Suite v23.011 in MicroStation v24.00.002.62. This stage included splitting by flight tracks (Fig. 3) and alignment using *Match Passes*. As a result, the mean 3D accuracy in both systems was below 1 cm, with vertical accuracy of 12 mm, supporting geometric consistency for subsequent analyses (See reports in Supplementary Material).

Noise in the point cloud was reduced using the *Smoothen and Remove Noise* tool, classifying as outliers those points with fewer than three neighbours within a 3 m radius. During the two evaluation dates, System A had 4.38% and 5.35% of points classified as noise, while System B registered 9.51% and 8.05%, respectively. Fig. 4 shows the noise-classified points overlaid on the LiDAR point cloud.

Finally, Ground points were then classified to generate the Digital Terrain Model (DTM). Using the remaining non-ground points, the Digital Surface Model (DSM) was produced, including vegetation and other above-ground features. The difference between these two models resulted in the Canopy Height Model (CHM), which was used to quantify the vertical structure of the forest vegetation, as show in Fig. 5.

2.3.2. Processing of passive sensor

The images captured using the MicaSense RedEdge-P sensor were processed in Agisoft Metashape Professional v2.2.1. Radiometric calibration was applied using a calibrated reflectance panel and records from the Downwelling Light Sensor (DLS2) to correct illumination variability between dates. Photogrammetric alignment was performed using high accuracy and ground control points (GCPs) were incorporated to geospatially adjust the orthomosaics. The geospatial adjustment achieved an approximate positional accuracy of 1–3 cm; additional details are provided in the Agisoft Metashape processing reports included in the Supplementary Material.

Based on the depth maps, a dense point cloud was generated, followed by the creation of a Digital Elevation Model (DEM). The multispectral orthomosaic was constructed over the DEM and enhanced through spectral fusion (pansharpening) using the panchromatic band to improve spatial resolution.

This process was performed using the Raster Calculator tool in Agisoft Metashape, applying the equations shown in Table 1 and enabling spectral transformations. The resulting product was exported as an optimized multiband raster with assigned index values in the transformed raster.

2.4. Analysis of derived products

Tree heights were derived from the Canopy Height Models (CHM) for each individual present in the evaluated systems. To validate

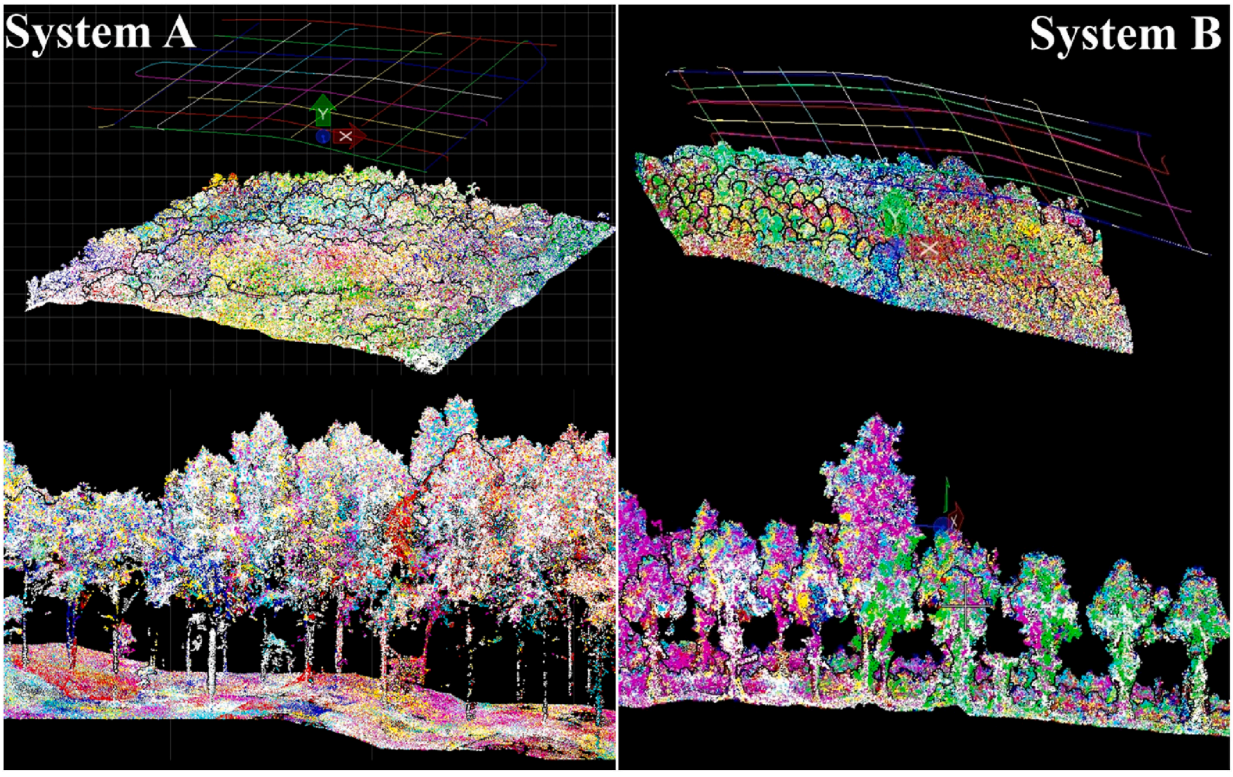

Fig. 3. Top and side views of the point cloud coloured by flight tracks. Each colour represents an individual flight line, allowing for verification of trajectory overlap and geometric consistency, as well as the use of two sensor angles.

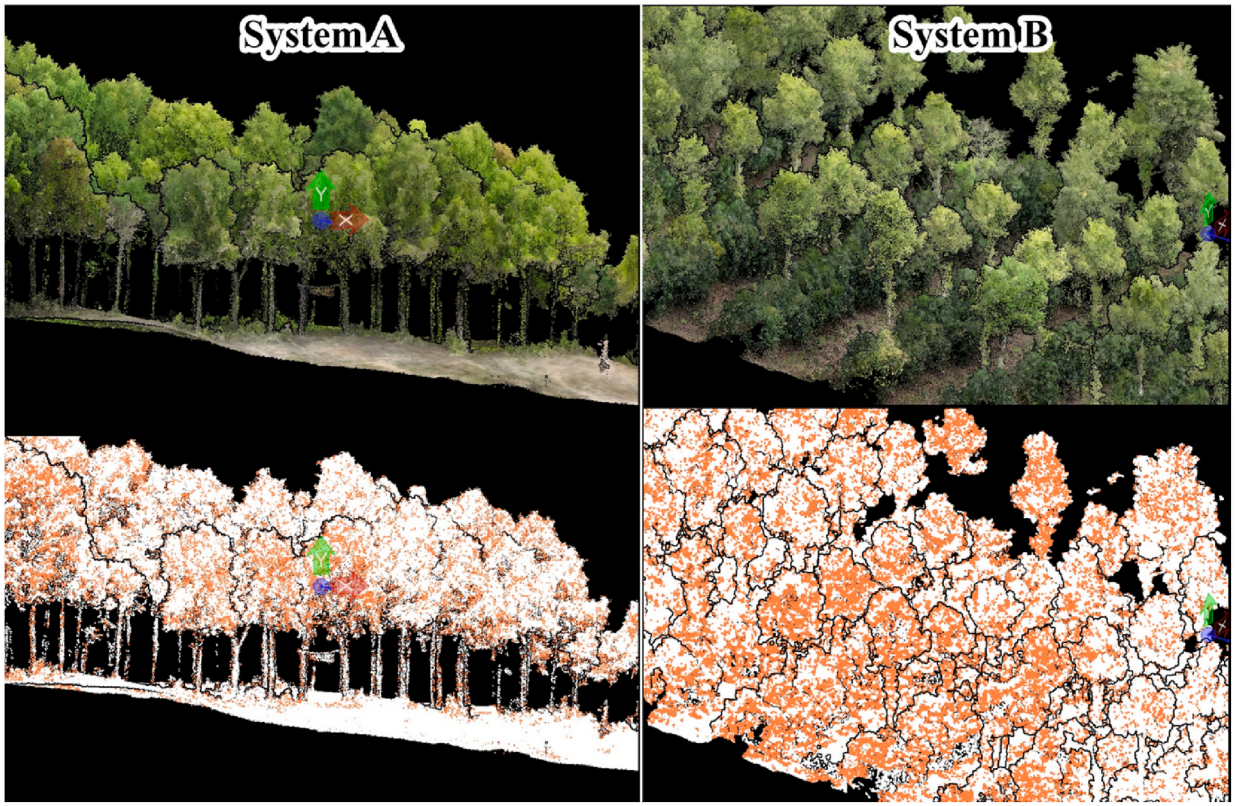

Fig. 4. Sections of the initial point cloud in both systems, where orange highlights the points identified as noise over the original distribution.

the accuracy of these estimations, direct field measurements were conducted using a Nikon Forestry Pro II laser hypsometer on ten selected trees per system. Agreement between LiDAR-derived heights and field measurements was first quantified using error metrics, including root mean square error (RMSE), mean absolute error (MAE), bias (mean error), and RMSE (%), calculated from paired observations of LiDAR- and hypsometer-based heights. In addition, a Bland–Altman analysis was performed to identify potential systematic bias and quantify the level of agreement between both methods.

$$RMSE = \sqrt{\frac{1}{n}\sum_{i=1}^{n}(P_i - O_i)^2}$$

$$MAE = \frac{1}{n}\sum_{i=1}^{n}|P_i - O_i|$$

$$Bias = \frac{1}{n}\sum_{i=1}^{n}(P_i - O_i)$$

$$RMSE\% = \left(\frac{RMSE}{\overline{O}}\right) \times 100$$

where: O_i is value observed is the observed tree height measured in the field with the hypsometer, P_i is the tree height estimated from the LiDAR-derived CHM, n is the number of paired observations, and $\overline{O}$ is the mean of the observed field heights.

Additionally, from the multispectral orthomosaics, eight spectral indices associated with canopy vigour and health were calculated. These included: Normalized Difference Vegetation Index (NDVI), Green NDVI (GNDVI), Modified Soil Adjusted Vegetation Index (SAVI), Enhanced Vegetation index (EVI), Chlorophyll Index - Red-Edge, Normalized Difference Red Edge Index (NDRE), Modified Triangular Vegetation Index (MTVI2), Red-Edge Triangulated Vegetation Index (RTVI Core). The equations used are presented in Table 2, where NIR refers to the Near Infrared band, and RE refers to the Red Edge band.

Finally, to evaluate the representativeness and redundancy of the spectral information, a Principal Component Analysis (PCA) was applied to the spectral index matrix, using values extracted from the full canopy coverage. This procedure allowed identification of the indices with the highest contribution to total variance and supported the selection of the most relevant variables for characterizing

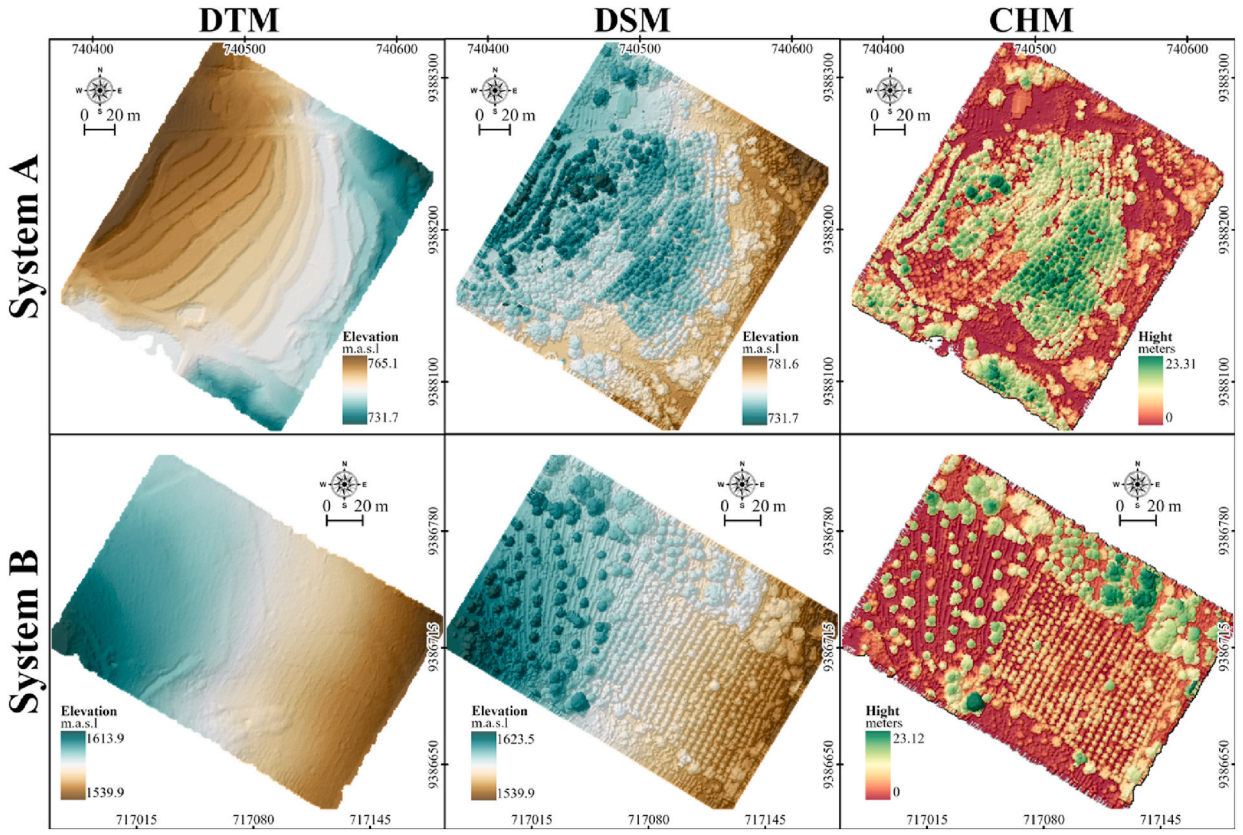

Fig. 5. Generation of DTM, DSM, and CHM for the two evaluated systems.

Table 1
Formulas used in Agisoft Metashape to perform spectral fusion.

Formula	New band
$B1*(B3 \ / \ (0.2*B1 + 0.2*B2 + 0.2*B4 + 0.2*B5 + 0.2*B6)) \ / \ 32768$	Blue
$B2*(B3 \ / \ (0.2*B1 + 0.2*B2 + 0.2*B4 + 0.2*B5 + 0.2*B6)) \ / \ 32768$	Green
$B4*(B3 \ / \ (0.2*B1 + 0.2*B2 + 0.2*B4 + 0.2*B5 + 0.2*B6)) \ / \ 32768$	Red
$B5*(B3 \ / \ (0.2*B1 + 0.2*B2 + 0.2*B4 + 0.2*B5 + 0.2*B6)) \ / \ 32768$	Red edge
$B6*(B3 \ / \ (0.2*B1 + 0.2*B2 + 0.2*B4 + 0.2*B5 + 0.2*B6)) \ / \ 32768$	Near Infrared

where: B1, B2, B3, B4, B5 and B6 correspond to the native bands: Blue, Green, Panchromatic, Red, Red Edge, and Near Infrared, respectively.

vegetation physiological responses.

3. Results

3.1. Structural assessment using LiDAR data

3.1.1. General structure of the evaluated systems

System A covered an area of 3.28 ha and recorded a total of 571,274,811 points. In contrast, System B covered 2.63 ha and recorded 489,051,593 points. The average elevation in System A was 753 m above sea level, while System B was located at an average elevation of 1578 m; as show in Fig. 6.

3.1.2. Growth estimation using LiDAR data

Fig. 7 shows the canopy height models (CHM) generated from the March (initial CHM) and July (final CHM) flights, as well as the difference raster (CHM change) between both periods. In System A, the average canopy height increased from 4.87 m to 5.30 m, representing a mean gain of 0.44 m. However, localized areas with significant height loss were identified, with minimum values reaching approximately −14.13 m, mainly in the northern and southern sectors of the system.

Table 2
Equations used to calculate the spectral indices.

Name	Formula	Reference
NDVI	$\frac{NIR - Red}{NIR + Red}$	Rouse et al. (1974)
GNDVI	$\frac{NIR - Green}{NIR + Green}$	Buschmann and Nagel (1993)
MSAVI	$\frac{1}{2}*\left[2*NIR + 1 - \sqrt{(2*NIR + 1)^2 - 8*(NIR - Red)}\right]$	Qi et al. (1994)
EVI	$2.5*\frac{NIR - Red}{NIR + 6*Red - 7.5*Blue + 1}$	Huete et al. (2002)
CiRE	$\frac{NIR}{RE} - 1$	Gitelson and Merzlyak (1998)
NDRE	$\frac{NIR - RE}{NIR + RE}$	Sims and Gamon (2002)
MTVI2	$\frac{1.5*[1.2*(NIR - Green) - 2.5*(Red - Green)]}{\sqrt{(2*NIR + 1)^2 - \left(6*NIR - 5*\sqrt{Red}\right) - 0.5}}$	Haboudane et al. (2004)
RTVI Core	$100*(NIR - RE) - 10*(NIR - Green)$	

In System B, a slight decrease in average canopy height was observed (from 5.12 m to 4.98 m), attributed to the removal of temporary vegetation—specifically maize—recorded during the first flight. This dynamic is reflected in the CHM change raster as extensive areas with negative values. Height gains were confined to the crowns of established trees, as indicated by localized positive values in the difference map.

To complement the analysis, Fig. 8 presents the canopy height kernel density estimation (KDE) for both the initial and final CHMs in each system (panels a and c), as well as the distributions of canopy height changes (panels b and d). In System A, the KDE curves revealed a bimodal structure, with two main peaks representing distinct vegetation groupings. In System B, three peaks were present in the initial assessment and two in the final, suggesting a simplification of vertical canopy structure over the evaluated period.

In both systems, a slight rightward shift of the curves was observed, indicating a general—albeit moderate—increase in canopy height, as previously estimated by the mean gains (0.44 m in System A and 0.15 m in System B). Furthermore, the change distributions (panels b and d) showed a high density around zero, reflecting the short interval between flights (four months) and the structural stability of most vegetation cover. However, System B exhibited a negative skew in the distribution, consistent with the loss of temporary vegetation observed in the field.

Additionally, Table 3 summarizes the descriptive statistics and key percentiles derived from the initial and final CHMs for both systems. In System A, there was an increase in the mean (from 4.87 m to 5.30 m) and in higher percentiles such as P95 and P99, indicating generalized growth, particularly among dominant individuals. In System B, although the median (P50) and P95 slightly increased, the mean exhibited a slight decrease. The negative skewness in both systems reflects the dominance of low-stature vegetation, while the negative kurtosis observed in System A suggests a flatter distribution compared to System B.

To complement the analysis of vegetation structural changes, Fig. 9 presents the relative canopy height change for both systems. In System A (panels a–c), the losses were concentrated in low vegetation and a few scattered forest individuals. In System B (panels d–f), structured areas of height reduction were evident, mainly due to the removal of maize crops and manual weeding operations. In both cases, the crowns of taller vegetation appear in whitish tones, indicating changes close to zero. This distribution aligns with the structural stability of permanent vegetation elements and confirms that significant variations occurred primarily in lower vegetation layers.

3.2. Spectral assessment using passive data

3.2.1. Spectral response of the evaluated systems

Fig. 10 presents the natural RGB composition and the corresponding spectral indices for both evaluated systems during the initial monitoring date. Each spectral index is displayed using colour scales ranging from low (red) to high (green) values, revealing distinct contrasts in spectral response across different zones within the systems.

In general, indices such as NDVI, EVI, or NDRE are typically associated with higher chlorophyll content or photosynthetic activity, while MSAVI and MTVI2 reflect variations in canopy density. These differences allow the identification of areas with greater foliar development. The central RGB image helps to spatially contextualize these patterns and compare them with the actual vegetation cover.

Table 4 presents the descriptive statistics for the eight spectral indices calculated during the initial evaluation of Systems A and B. NDVI exhibited relatively low standard deviation, particularly in System B, where the Coefficient of Variation (CV) was 12.4%, suggesting reduced spatial variability—likely due to saturation in densely vegetated areas. In contrast, indices such as MTVI2, RTVI Core, and CiRE showed higher variability levels (CV $>$ 30% in both systems), indicating greater sensitivity to canopy structural differences and potential plant health conditions.

Notably, the CiRE index showed an extremely high coefficient of variation in System A (CV = 580.5%), driven by outliers and a highly heterogeneous spectral response. This highlights the importance of conducting a more detailed analysis within representative subzones.

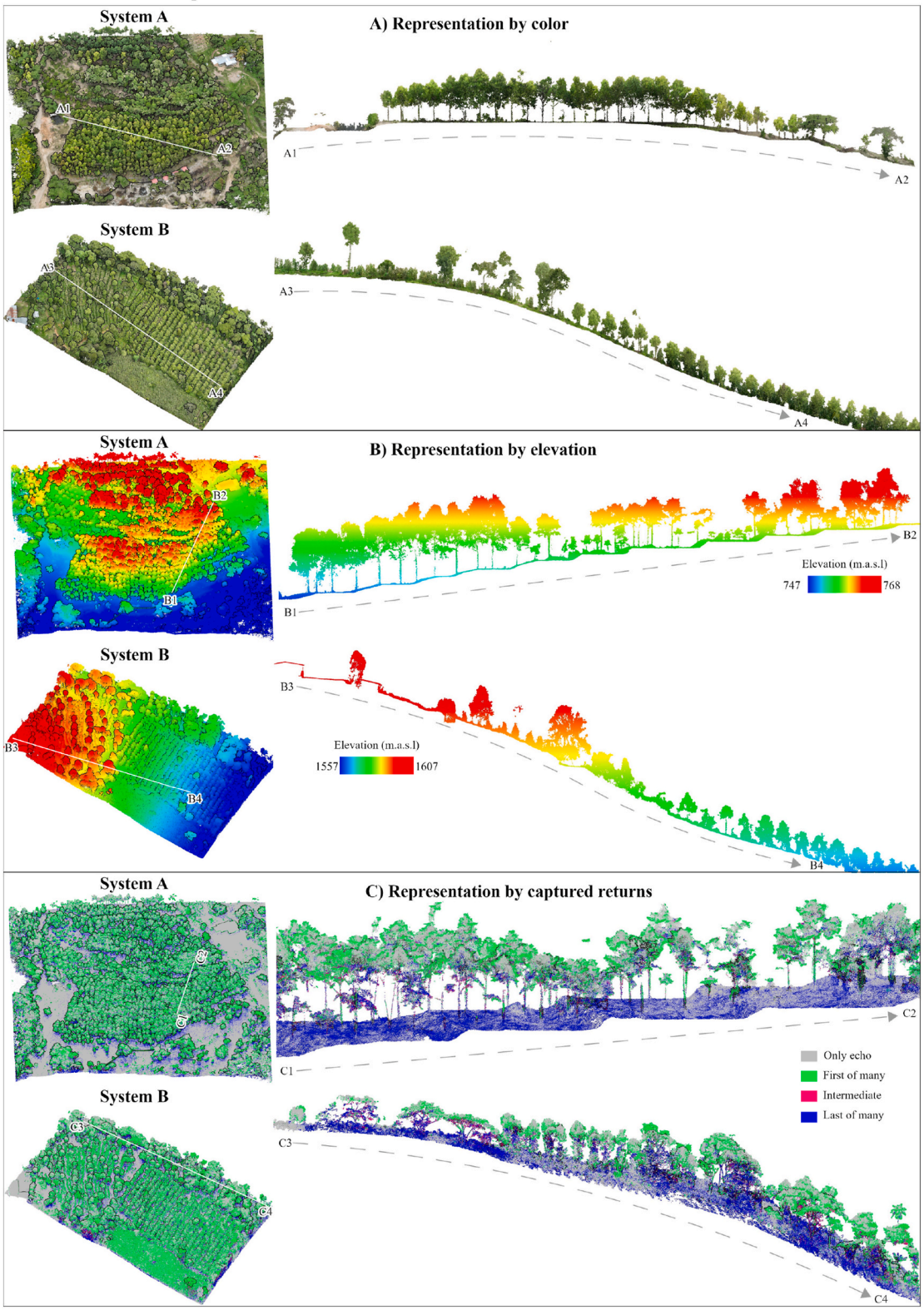

Fig. 6. Point cloud visualization of the evaluated systems: (a) colorized RGB view, (b) elevation-based rendering, and (c) classified LiDAR returns.

3.2.2. Analysis of the representativeness of spectral indices

Fig. 11 shows the distribution and relationships of the spectral indices extracted from the forest cover of Systems A (sky blue) and B (orange). Notable associations were observed, such as the strong correlation between MSAVI and EVI—both sensitive to canopy structure—as well as between GNDVI and NDRE, which are linked to foliage content and vegetation health. Likewise, the relationship between MTVI2 and RTVI Core confirmed their convergence in detecting structural variations. Visually, both systems exhibited similar patterns in many relationships, although slight shifts in magnitude suggest subtle functional or structural differences.

Because some relationships did not exhibit strictly linear patterns, Fig. 12 presents the Spearman correlation matrix, which does not assume linearity in the data. In System A, strong correlations were identified between MSAVI–EVI ($\rho = 0.99$), GNDVI–NDRE ($\rho = 0.91$), and MTVI2–RTVI Core ($\rho = 0.92$), indicating structural and functional coherence. In System B, these associations persisted, although with slight variations in coefficient magnitudes. Notably, a weaker correlation was observed between NDVI and GNDVI ($\rho = 0.51$), suggesting potential differences in the sensitivity of these indices to physiological or structural changes.

Fig. 13 shows the Principal Component Analysis (PCA) applied to the data extracted from the eight spectral indices over the forest cover. Despite the correlations between variables (Fig. 12), the PCA factor loadings indicated that all indices contributed to explaining variance to different degrees. Specifically, the first two principal components accounted for 94.25% and 94.86% of the total variance in Systems A and B, respectively.

In System A (Fig. 13A), the first principal component (PC1) explained 72.25% of the variance, dominated by strong positive loadings of GNDVI, MSAVI, EVI, NDRE, and MTVI2, reflecting both structural and functional sensitivity. PC2 (22.0%) showed strong negative loadings for GNDVI, CiRE, and NDRE, mainly associated with differences in foliar health. In System B (Fig. 13B), PC1 explained 52.7% of the variance, with high positive loadings more evenly distributed across indices, while PC2 (42.16%) exhibited marked contrasts between structural indices (MSAVI, MTVI2) and functional indices (NDVI, EVI, NDRE), indicating a more complex differentiation in the spectral patterns of the system.

Finally, the discriminative capacity of the spectral indices is shown in Fig. 14, representing their spatial variation along transects defined in three representative sections of the systems during the initial monitoring date. Only the most representative indices with comparable value ranges are presented: MSAVI and MTVI2, due to their structural sensitivity, and GNDVI and NDRE, for their functional association with foliage content and vegetation health. For a more detailed analysis of each index, see Annex 1.

The selected indices adequately capture both the structural and functional aspects of the systems. MSAVI and MTVI2 respond more clearly to canopy density, whereas GNDVI and NDRE highlight areas with high chlorophyll content, even in zones with lower structural cover. This behavior makes it possible to distinguish between physical limitations and favorable functional conditions, thereby avoiding misinterpretations in multitemporal analyses, such as confusing low biomass with physiological decline.

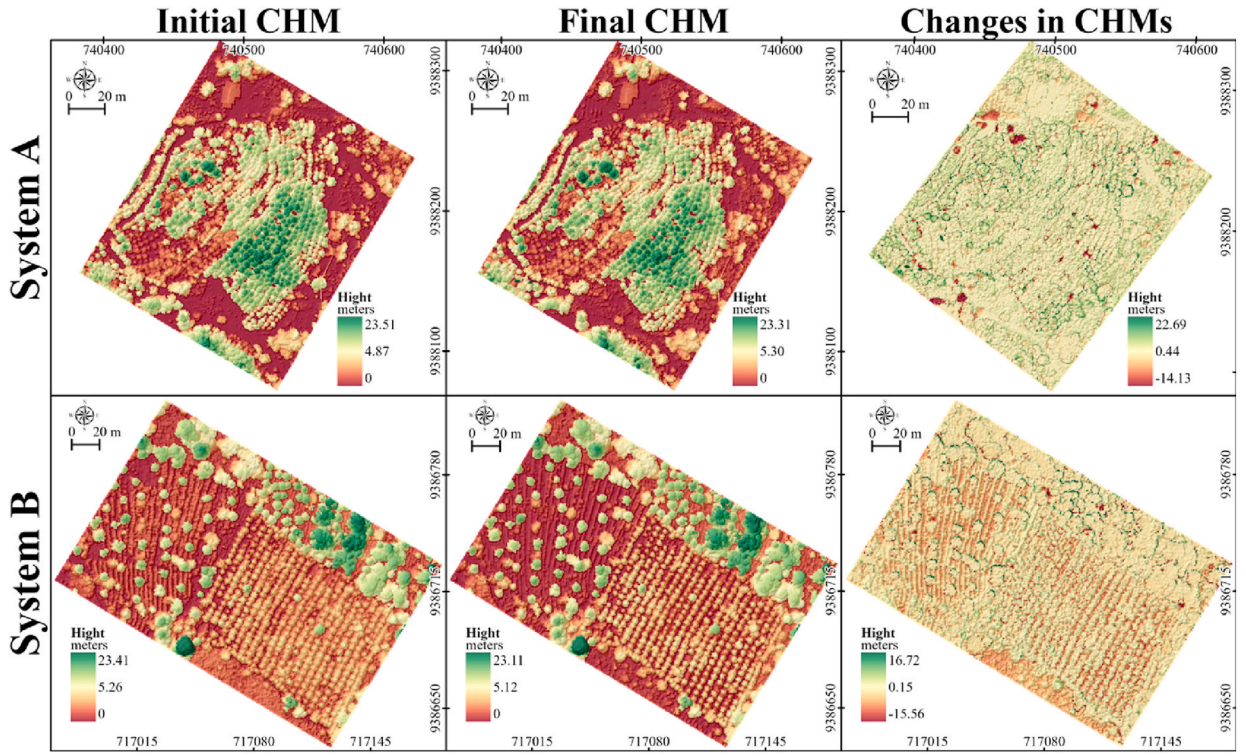

Fig. 7. Canopy height models and differences for forest systems A and B.

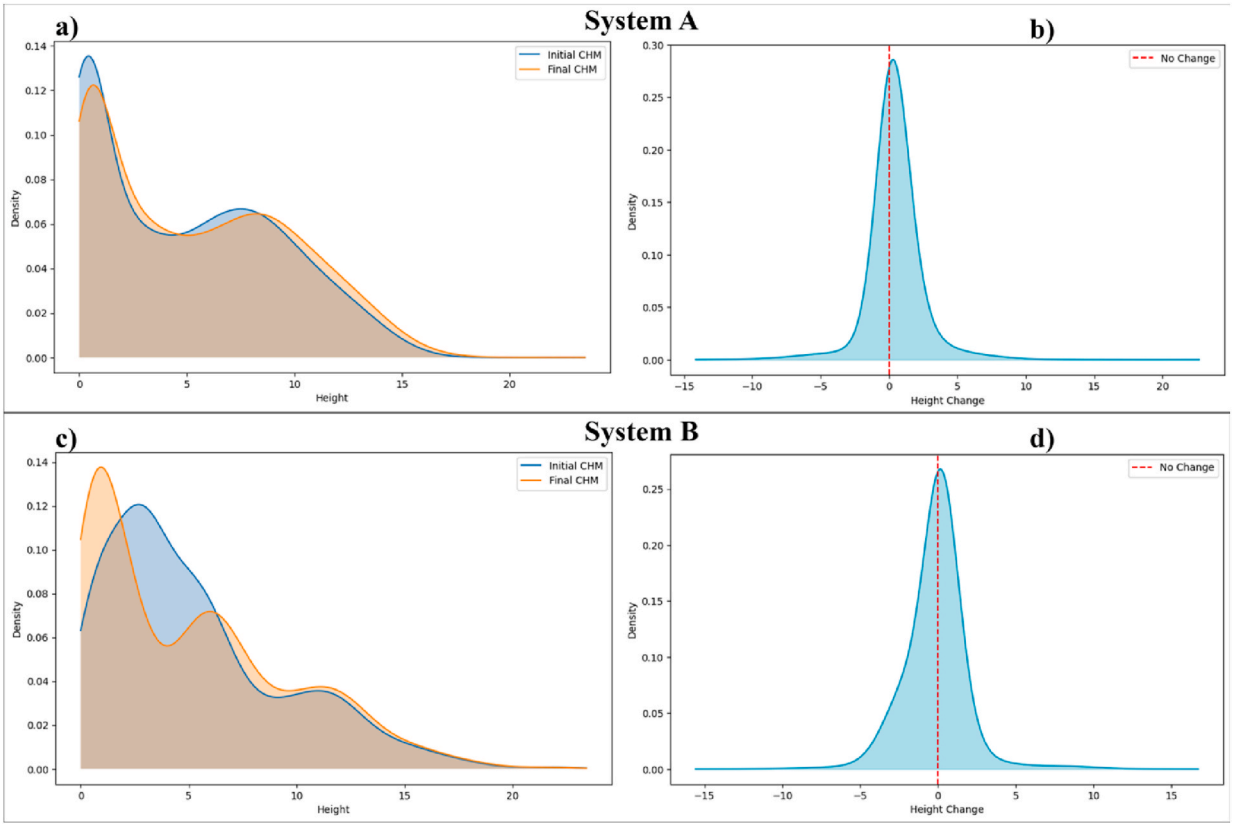

Fig. 8. Canopy height density distributions and changes between evaluations.

Table 3
Descriptive statistics and canopy height percentiles (m) derived from the initial and final CHMs for Systems A and B.

	Date	Mean	SD	Skewness	Kurtosis	Percentiles (m)						
						P10	P25	P50	P75	P90	P95	P99
System A	Initial	4.87	4.27	0.47	−0.96	0.10	0.43	4.25	8.27	11.02	12.46	14.50
	Final	5.30	4.41	0.45	−0.94	0.15	1.03	4.68	8.84	11.60	13.01	15.12
System B	Initial	5.26	4.18	1.03	0.55	0.63	2.18	4.16	7.28	11.73	13.39	17.03
	Final	5.12	4.57	0.84	−0.09	0.33	1.04	4.26	7.88	12.0	13.63	17.20

3.3. Validation of LiDAR measurements

The height distributions obtained with the hypsometer and LiDAR data showed differentiated patterns depending on the system and evaluation date (Fig. 15). An increase in canopy height was observed from March to July in both systems and for both measurement methods. The distributions exhibited positive skewness, particularly in System A in July, indicating a higher concentration of individuals with shorter heights and a tail extending toward taller individuals. The LiDAR-derived height distributions displayed comparable patterns of dispersion and central tendency to the hypsometer measurements within each date and system, although slight variations in distribution shape were observed.

In agreement with these patterns, a strong correlation was observed between both measurement methods, as shown in Fig. 16. System A presented high coefficients of determination ($R^2 = 0.95$ in March and $R^2 = 0.96$ in July), while System B also showed strong correlations, albeit slightly lower ($R^2 = 0.88$ in March and $R^2 = 0.90$ in July). Slopes close to unity indicate strong concordance between methods, reinforcing the validity of LiDAR estimates for characterizing canopy height.

In addition to the correlation analysis, error metrics were calculated to quantify agreement in absolute and relative terms (Table 5). Across all validation trees and both campaigns ($n = 40$), LiDAR-derived heights showed an RMSE of 0.197 m, MAE of 0.160 m, and a mean bias of +0.088 m, corresponding to an RMSE of 2.76%. At the campaign level, RMSE% ranged from 2.32% (March) to 3.07% (July), indicating low relative error and supporting the consistency of LiDAR-based estimates across systems and dates.

As illustrated in Figs. 15 and 16, the validation individuals showed comparable distribution patterns and a strong linear relationship between methods. To complement this evaluation, Table 5 summarizes absolute and relative error metrics, and Fig. 17

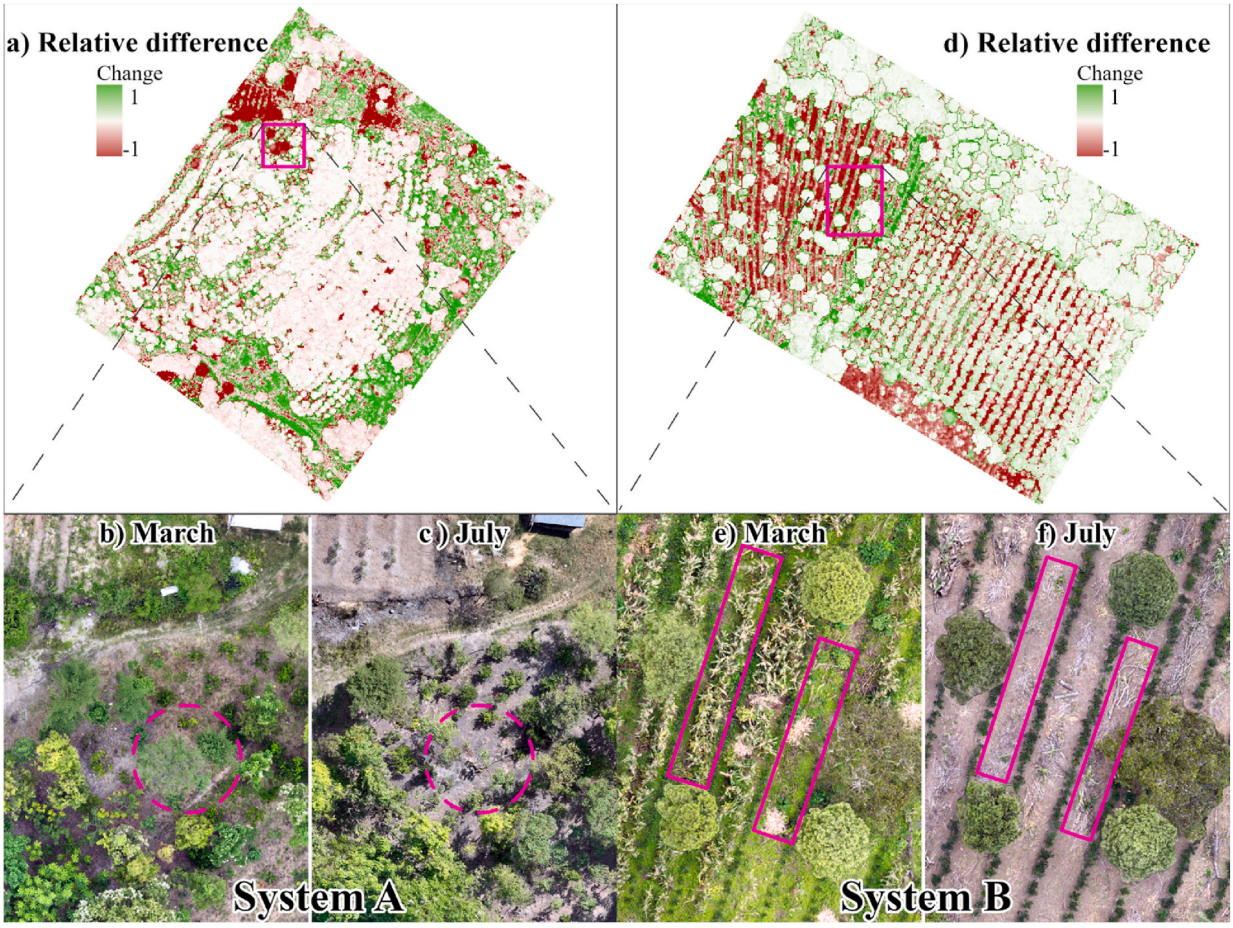

Fig. 9. Relative canopy height changes between March and July for Systems A and B.

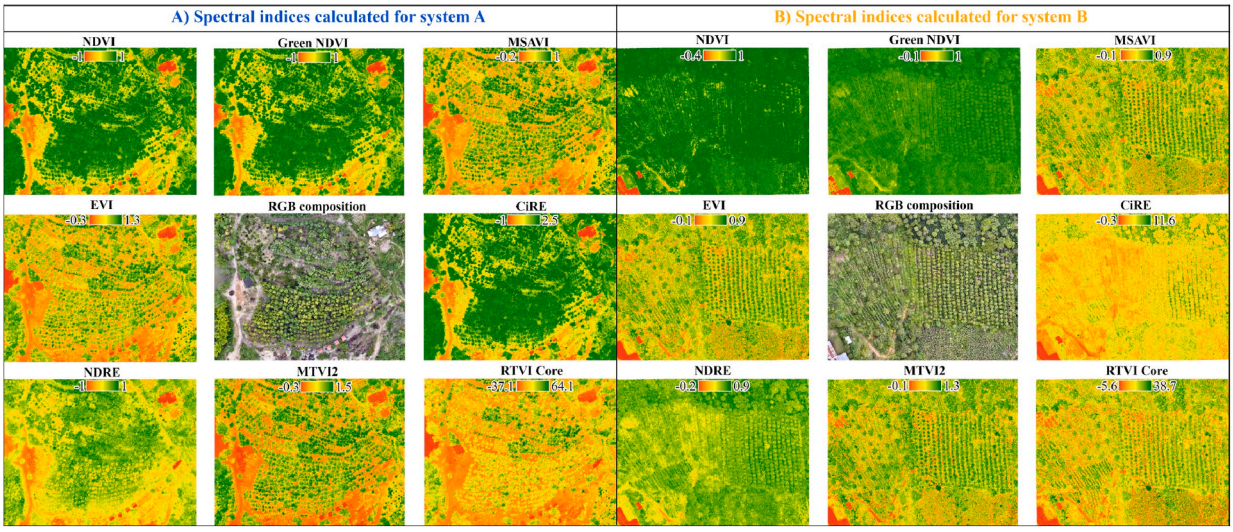

Fig. 10. Spectral indices calculated during the first evaluation of Systems A and B.

Table 4
Descriptive statistics of spectral indices calculated over the full extent of Systems A and B.

Index	System A					System B				
	Mean	SD	Min	Max	CV	Mean	SD	Min	Max	CV
NDVI	0.71	0.23	−1	1	32.4	0.89	0.11	−0.4	1	12.4
GNDVI	0.67	0.16	−1	1	23.9	0.81	0.09	−0.1	1	11.1
MSAVI	0.48	0.24	−0.2	1	50	0.46	0.16	−0.1	0.9	34.8
EVI	0.51	0.25	−0.3	1.3	49	0.47	0.15	−0.1	0.9	31.2
CiRE	1.49	8.65	−1	2.5	580.5	2.84	1.03	−0.3	11.6	36.3
NDRE	0.41	0.12	−1	1	29.3	0.57	0.09	−0.2	0.9	15.8
MTVI2	0.49	0.29	−0.3	1.5	59.2	0.52	0.18	−0.1	1.3	34.6
RTVI Core	17.69	9.27	−37.1	64.1	52.4	16.41	5.93	−5.6	38.7	36.1

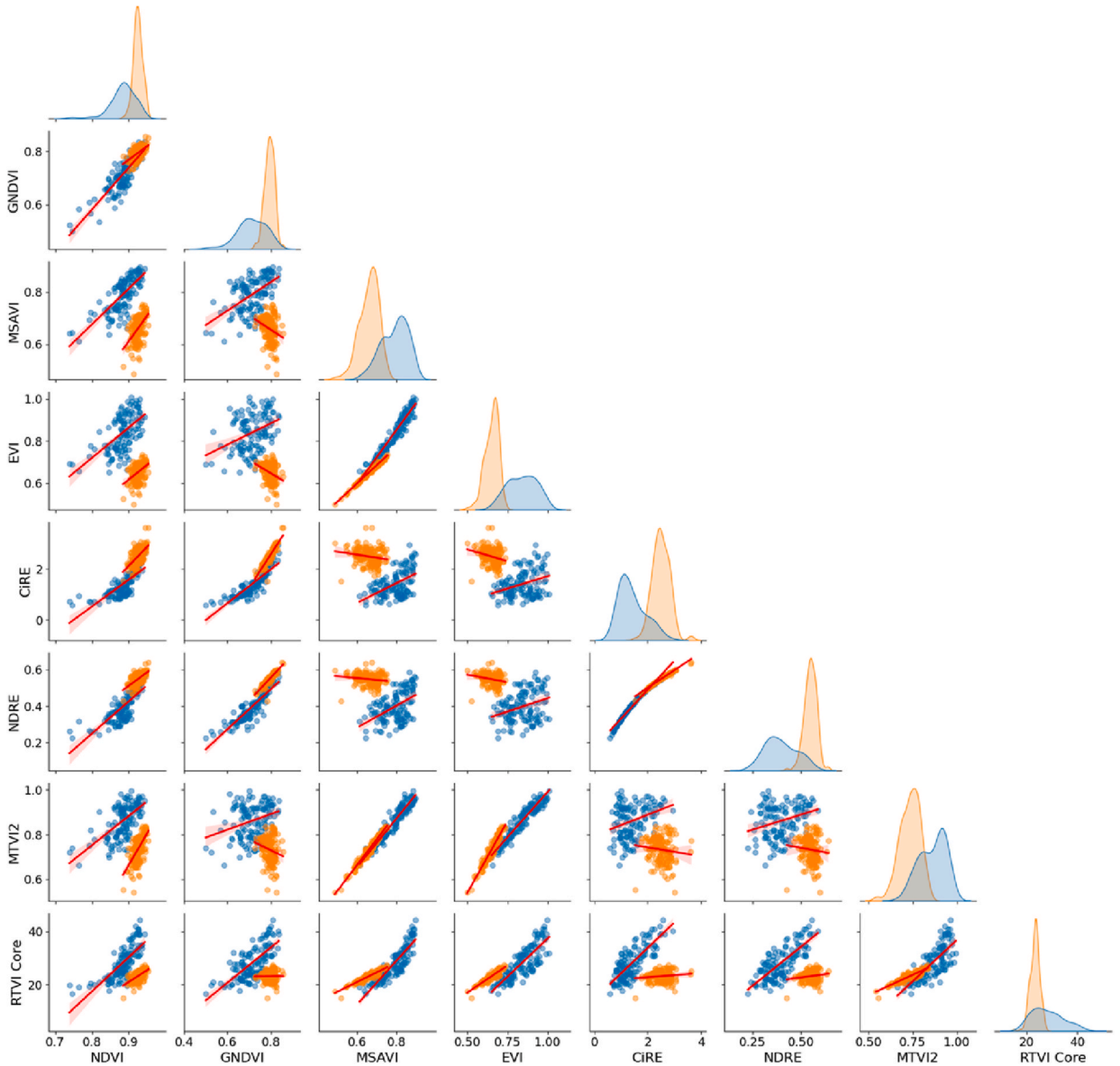

Fig. 11. Distribution and relationships of spectral indices in Systems A (sky blue) and B (orange) on March 5, 2025.

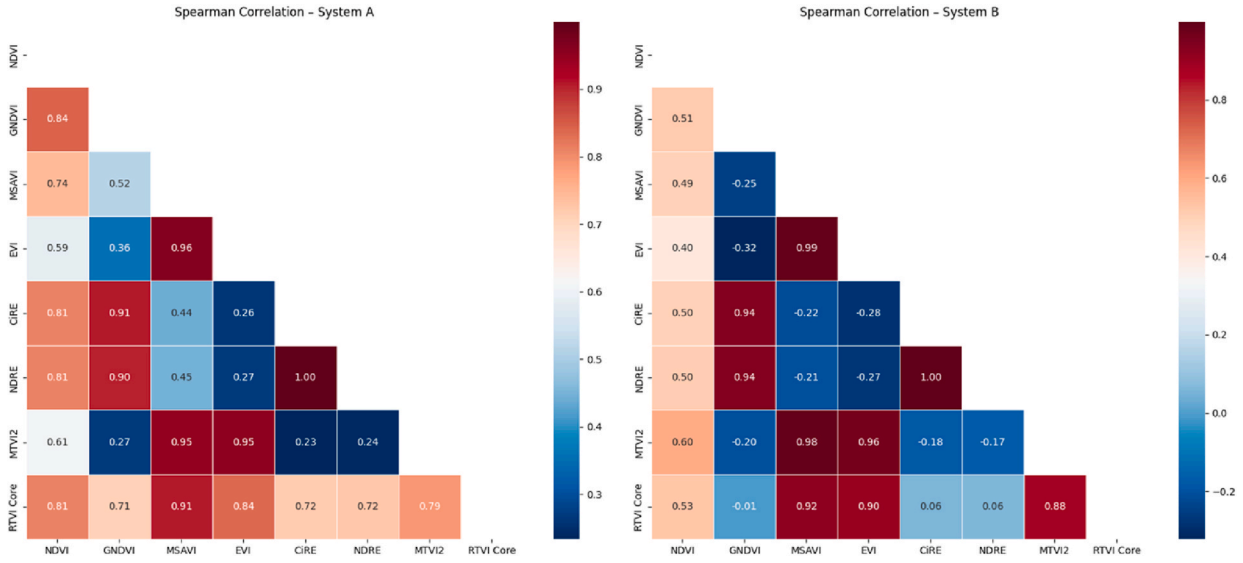

Fig. 12. Spearman correlation matrix of the evaluated spectral indices.

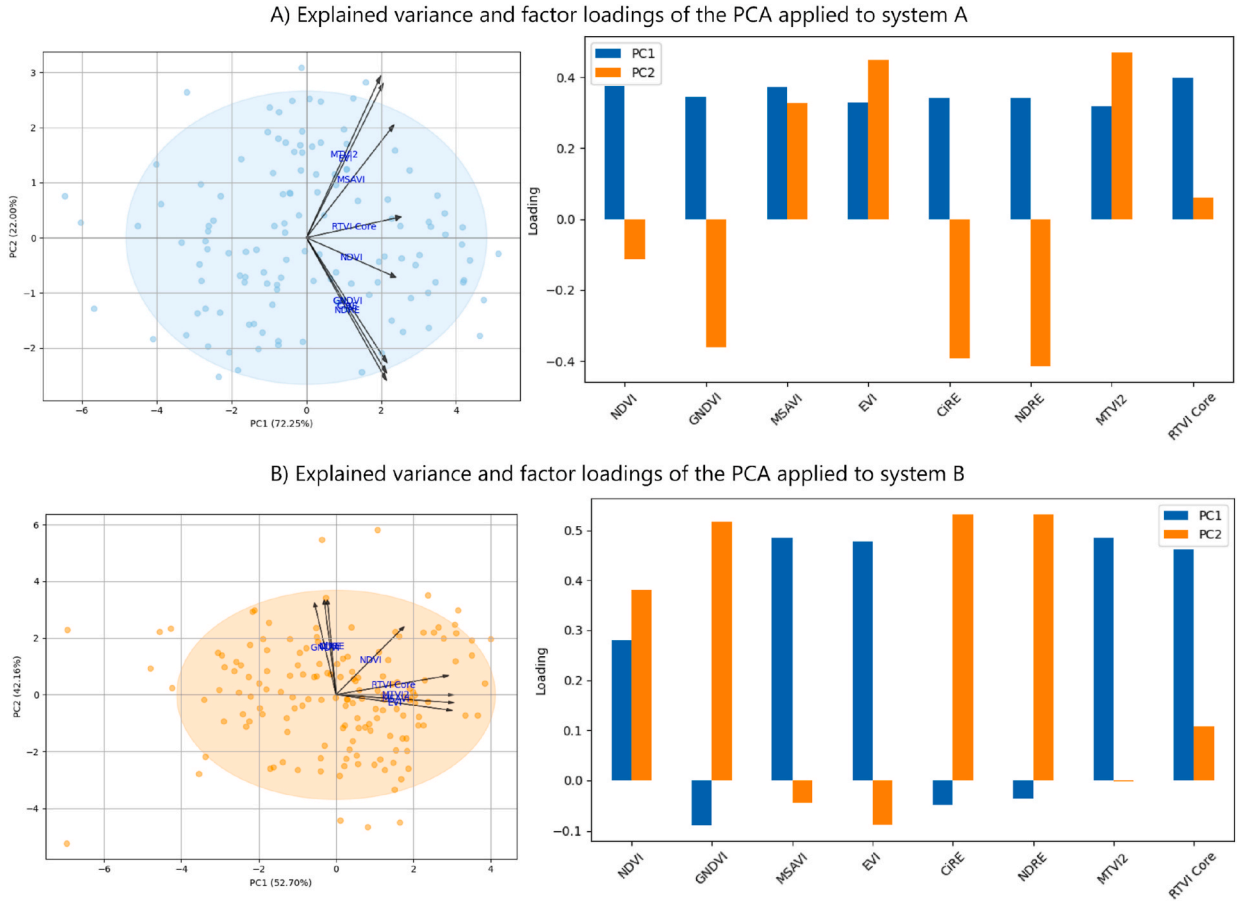

Fig. 13. Principal Component Analysis of the spectral indices calculated for each system.

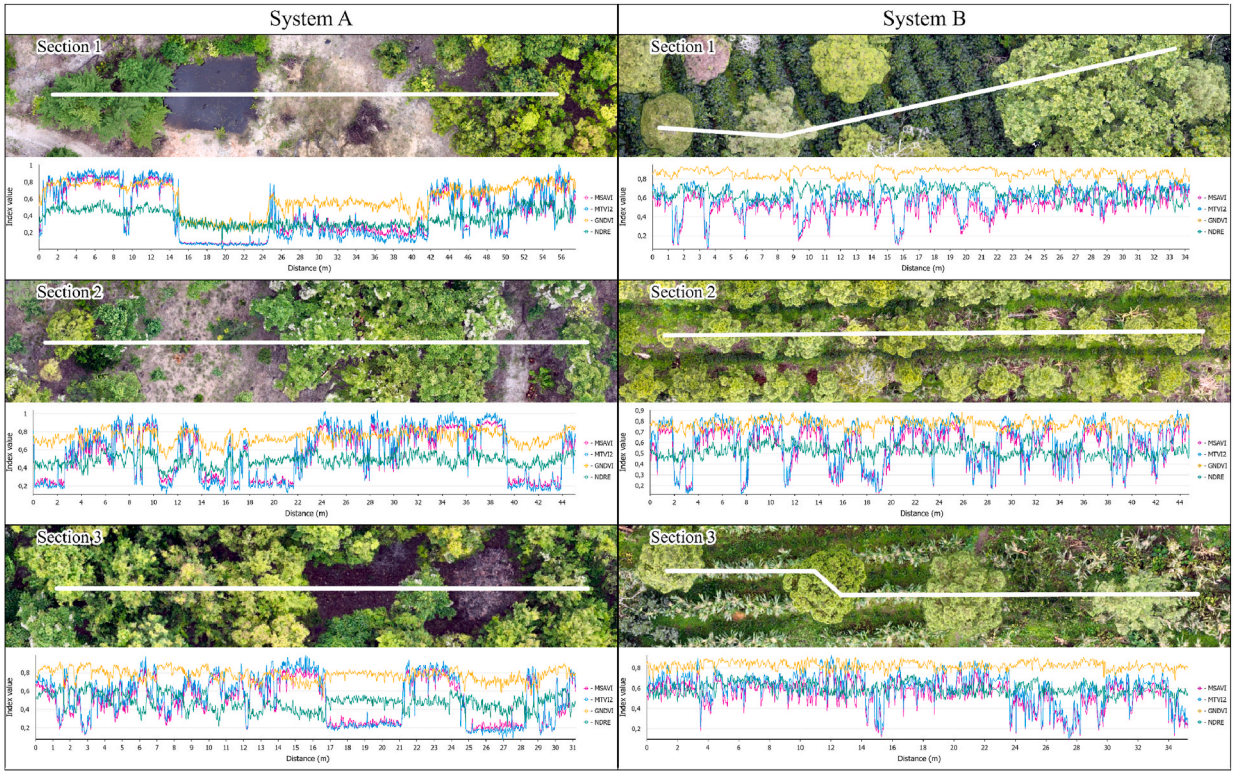

Fig. 14. Spectral variation along linear transects across three sections of Systems A and B.

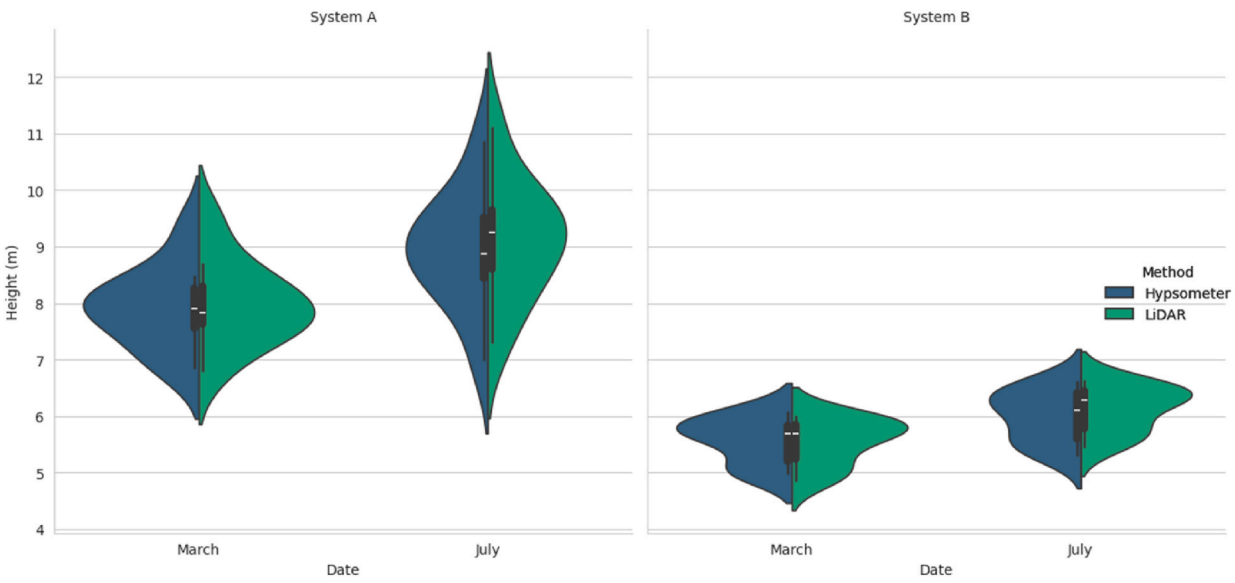

Fig. 15. Height distributions obtained with hypsometer and LiDAR for the evaluated systems in March and July 2025.

presents the Bland–Altman concordance analysis. The mean difference (LiDAR – Hypsometer) was 0.09 m, suggesting a slight systematic bias in which LiDAR tends to overestimate heights compared to the hypsometer on average. The limits of agreement were −0.26 and 0.44 m, indicating the range within which most of the observed differences lie. Dispersion remained relatively constant across the range of averages, suggesting the absence of proportional error. However, greater variability was observed in System B and in the July measurements, although values remained within the agreement limits.

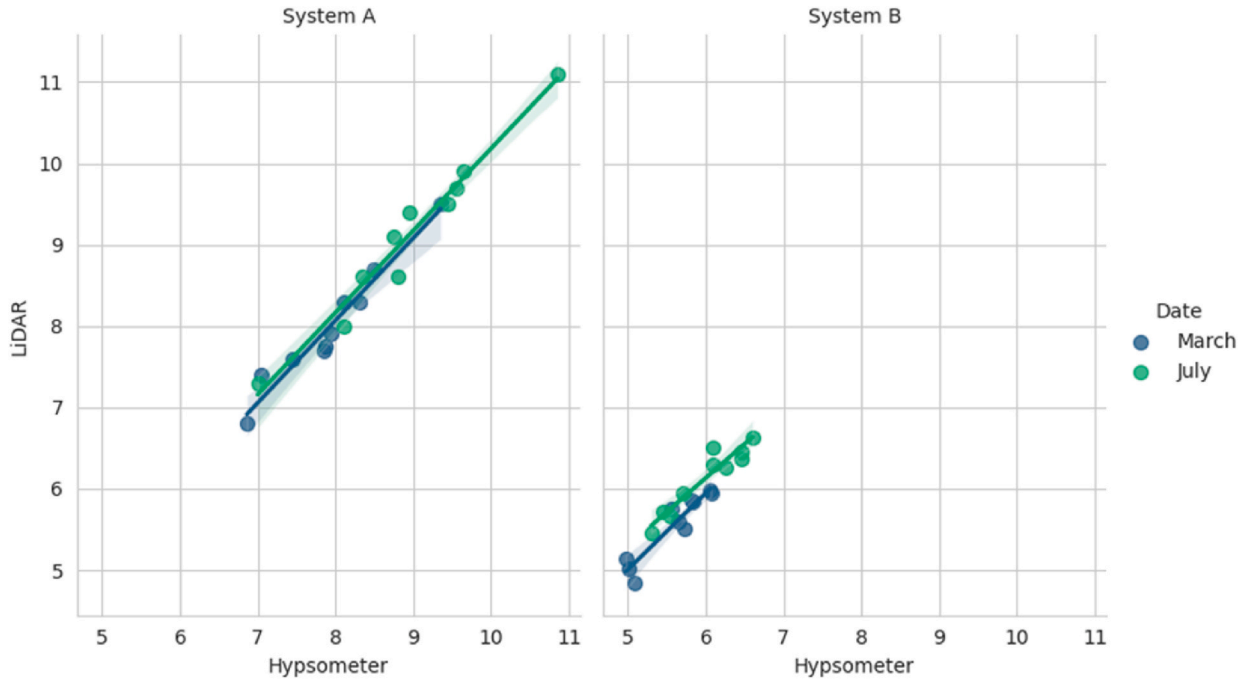

Fig. 16. Relationship between hypsometer-measured and LiDAR-estimated heights in Systems A and B during March and July 2025.

Table 5
Accuracy assessment metrics for LiDAR-derived tree heights (CHM-based) against field hypsometer measurements across systems and evaluation campaigns.

Campaign	System	n	RMSE (m)	MAE (m)	Bias (m)	RMSE (%)
March	A	10	0.172	0.143	+0.070	2.17
March	B	10	0.140	0.111	−0.028	2.51
March	Combined	20	0.157	0.127	+0.021	2.32
July	A	10	0.260	0.235	+0.175	2.91
July	B	10	0.194	0.150	+0.134	3.24
July	Combined	20	0.230	0.193	+0.155	3.07
All campaign	Combined	40	0.197	0.160	+0.088	2.76

4. Discussion

Zhang et al. (2024) demonstrated, using ray tracing in a voxel grid, that the integrity of sampling in UAV-mounted LiDAR systems mainly depends on pulse density and scan angle. They also identified missed impacts, canopy occlusion, and unscanned gaps as the primary causes of return loss. In this study, an acquisition configuration was applied to mitigate these limitations, using a sampling rate of 240 kHz, five returns, and a double-grid flight plan with scan angles of 90° and 45°. This combination increased effective coverage and improved the three-dimensional representation of the evaluated forest systems (Fig. 6).

From airborne laser scanning (ALS) data, vertical attributes such as canopy height, layer extension, and coverage can be derived with high concordance to field measurements (Morsdorf et al., 2010). However, pre-processing of the raw data is necessary. Therefore, through the Terra Scan and Terra Match modules in Terra Solid v.23.011, trajectory splitting and adjustment were performed (Fig. 3), a step that was critical to ensure geometric consistency, a fundamental requirement when generating accurate point clouds for monitoring applications (Sun et al., 2023).

Noise reduction in the point cloud was indispensable for both systems, representing 5% and 8% of the total points in Systems A and B, respectively (Fig. 4). This quality control had a direct impact on the accuracy of the derived products by minimizing spurious artifacts. Although advanced filtering approaches integrating full-waveform LiDAR, hyperspectral imagery, and deep learning have been reported (Luo et al., 2023), most studies agree that the quality of initial filtering directly determines the reliability of derived products, particularly in forest environments.

The canopy height models (CHM) and canopy height density analyses (Figs. 7 and 8) revealed contrasting dynamics between the evaluated systems. System A recorded a moderate increase in mean canopy height (0.44 m over four months), while System B showed a slight decrease, mainly due to the removal of temporary maize crops. These results align with Seidel et al. (2021), who documented marked differences in structural complexity among European agroforestry systems, highlighting that the presence and management of

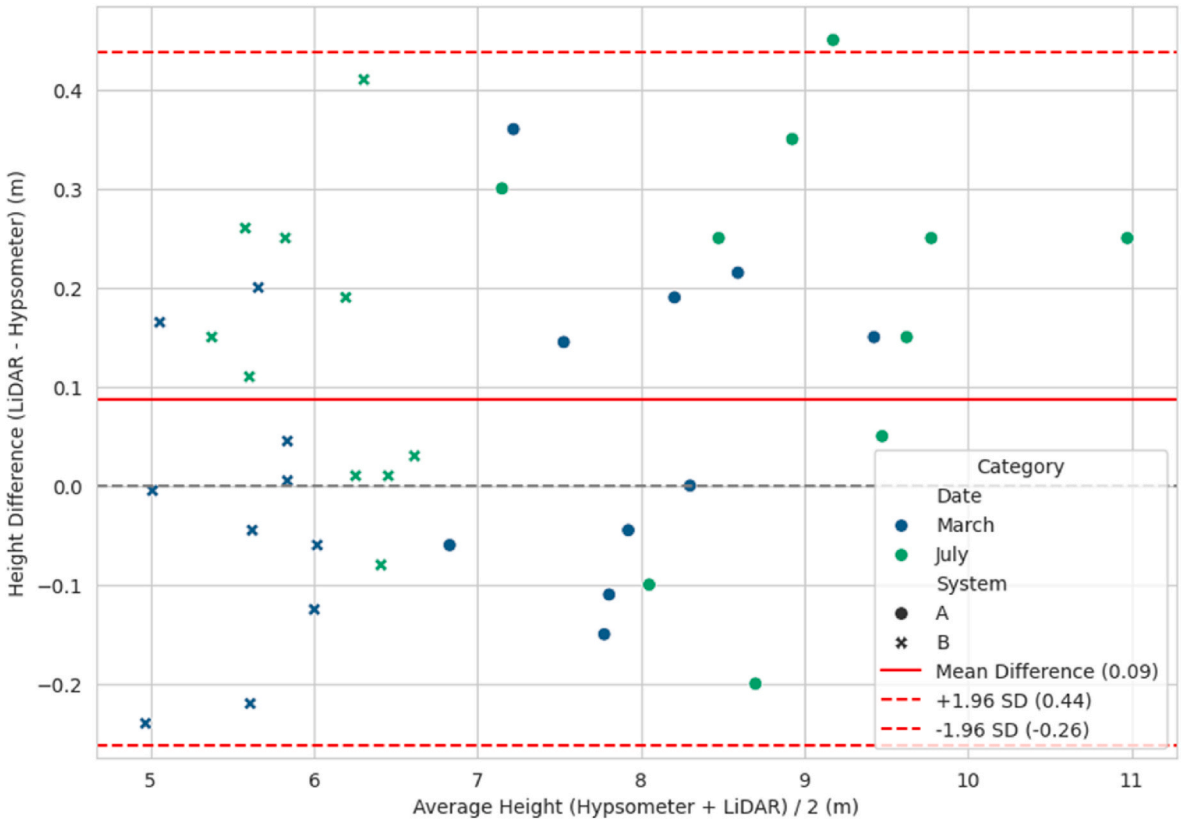

Fig. 17. Bland–Altman concordance analysis between hypsometer and LiDAR measurements of forest tree heights in March and July 2025.

agricultural components strongly influence metrics such as understory density and vertical diversity. In addition, relative canopy height differences allowed the detection of specific regeneration and canopy loss zones (Fig. 9), emphasizing the capacity of LiDAR to discriminate microstructural changes relevant for management planning.

The percentile analysis of canopy height showed a significant increase in the dominant canopy of System A (from 0.40 m to 0.60 m), whereas System B presented smaller variations (from 0.17 m to 0.30 m). This difference can be explained by species composition: System A was dominated by *Eucalyptus saligna* and *Calycophyllum spruceanum*, both fast-growing species, while System B was dominated by *Retrophyllum rospigliosii*, a slow-growing species (Ramírez et al., 2021; Restrepo and Alviar, 2010).

High percentiles are recognized as robust metrics for characterizing structural dynamics in multistratified ecosystems (Song et al., 2024). However, the Bland–Altman analysis revealed a slight systematic bias, with LiDAR tending to overestimate heights by +9 cm compared to the hypsometer. This phenomenon can be attributed to the sensor's higher sensitivity to dominant crowns and the geometry of multiple returns.

The integration of LiDAR and multispectral data improves the estimation of physiological attributes and reduces ambiguity in result interpretation (Chen et al., 2022; Wang et al., 2023). In our case, this integration enabled a comprehensive characterization of the structure and functionality of Systems A and B. The eight evaluated indices exhibited differentiated behaviours: MSAVI and MTVI2 were more sensitive to canopy structural variation, while GNDVI and NDRE were closely associated with chlorophyll content and photosynthetic vigour. The results of this study confirm the discriminative capacity of spectral indices (Fig. 14), allowing users to select the most suitable index depending on the analysis objective, whether focused on functionality or structure. This facilitates more precise evaluations in heterogeneous agroforestry systems, where monitoring based on one-dimensional data is limited.

The application of pansharpening enhanced the spatial resolution of orthomosaics, maximizing the capacity to discriminate fine-scale patterns of spectral and functional response (Wu et al., 2023). This technique is also effective in multistratified systems of high structural complexity, where separating canopy metrics across strata is critical (Fig. 10). Furthermore, the integration of a PCA on the spectral indices made it possible to identify key relationships and reduce redundancy, optimizing the selection of representative metrics for future evaluations. These methodological approaches open the door to developing advanced monitoring protocols that integrate multispectral data and metrics derived from multivariate analyses for landscape-scale studies.

LiDAR penetration in dense canopy areas was lower than expected, although this limitation was partially mitigated by the double scan-angle configuration. The short temporal interval between evaluations constrained the detection of subtle changes, yet this limitation was addressed through KDE distributions and relative difference maps, which allowed visualization of fine-scale dynamics that would not be apparent through a basic analysis. Likewise, the limited number of validation individuals introduces uncertainty, although the consistency with hypsometer measurements and the high coefficients of determination supports the robustness of LiDAR height estimates.

The capacity of LiDAR to generate high-quality Digital Terrain Models (DTMs) was evident in its accuracy in detecting land-use changes, such as in System A, which was previously a rice field and is now forested (Fig. 5). Similarly, Leitold et al. (2015) reported an airborne LiDAR-derived DTM with a mean error of 0.97 m and a bias of only 0.19 m compared to high-precision GNSS measurements. These results reinforce that LiDAR technology is a superior tool for accurately characterizing terrain in multistratified ecosystems and monitoring changes in land cover.

Therefore, this study demonstrates that the integration of LiDAR and multispectral data provides a robust strategy for simultaneously evaluating structural and functional attributes in agroforestry systems. At an applied level, the results support the proposal of optimized monitoring protocols to improve the early detection of structural and physiological changes in multistratified systems. However, although accuracy and quality-control indicators were incorporated across different stages of the workflow, this study did not implement a formal stepwise uncertainty propagation analysis; thus, this remains a key limitation that should be addressed in future research to strengthen the interpretability and transferability of the framework. Future research should incorporate longer temporal series to capture dynamics at different phenological scales and extend validation to more heterogeneous agroforestry landscapes, where the variability of associated crops poses additional challenges. Likewise, we recommend exploring the potential of machine learning models and hybrid approaches integrating LiDAR, multispectral, and radar data. Because this is a case study, evaluating these methodologies in additional sites and regional contexts will be necessary to assess the feasibility of scaling monitoring applications and to support the development of standardized and transferable protocols for the sustainable management of agroforestry systems in diverse productive environments.

5. Conclusions

This study demonstrates the feasibility of integrating UAV-LiDAR and multispectral imagery for multitemporal monitoring of structural and spectral vegetation proxies in a heterogeneous tropical agroforestry context. The main contribution is methodological, providing an operational workflow for deriving, integrating, and validating canopy-level indicators under complex canopy conditions. The results support the use of this approach as a transferable monitoring strategy for similar systems; however, because this is a case study, broader generalization and regional scaling should be considered with caution and require validation across additional sites, species compositions, and environmental conditions.

The multitemporal analysis revealed contrasting dynamics between the systems, with greater growth in System A, dominated by fast-growing forest species, and a slight structural reduction in System B, associated with the removal of temporary maize crops. High percentiles (P95, P99) and density distributions proved to be solid metrics for detecting vertical structural changes, while validation against field measurements confirmed the reliability of LiDAR estimates, with correlations above 0.9 and a minimal systematic bias (+9 cm).

Spectral indices also revealed differentiated patterns of photosynthetic vigour and canopy density, with MSAVI and MTVI2 being more sensitive to canopy structure, and GNDVI and NDRE closely linked to foliage content. The use of pansharpening and PCA optimized the discrimination of patterns and reduced redundancy.

CRediT authorship contribution statement

Teiser Sánchez-Fuentes: Writing – original draft, Visualization, Validation, Software, Methodology, Investigation, Formal analysis, Data curation, Conceptualization. **Darwin Gómez-Fernández:** Writing – review & editing, Visualization, Methodology, Investigation, Formal analysis, Conceptualization. **Jorge A. Fernandez-Jibaja:** Writing – review & editing, Visualization, Validation, Software, Methodology, Investigation, Data curation. **Jhon F. Oblitas-Troyes:** Methodology, Investigation, Formal analysis, Data curation, Conceptualization. **Beimer Chuquibala-Checan:** Methodology, Investigation, Formal analysis, Data curation. **Josué Tafur-Culqui:** Investigation, Formal analysis, Data curation. **Rosalia Quichua-Baldeon:** Investigation, Formal analysis, Data curation. **Victor H. Taboada-Mitma:** Resources, Project administration, Methodology, Investigation, Funding acquisition. **Daniel Tineo:** Resources, Project administration, Methodology, Funding acquisition, Formal analysis, Data curation. **Malluri Goñas:** Resources, Project administration, Methodology, Investigation, Funding acquisition, Formal analysis, Data curation. **Nilton Atalaya-Marin:** Supervision, Software, Resources, Project administration, Methodology, Investigation, Funding acquisition, Formal analysis, Data curation, Conceptualization.

Ethics in publishing statement

This research presents an accurate account of the work performed, all data presented are accurate and methodologies detailed enough to permit others to replicate the work.

This manuscript represents entirely original works and or if work and/or words of others have been used, that this has been appropriately cited or quoted and permission has been obtained where necessary.

This material has not been published in whole or in part elsewhere.

The manuscript is not currently being considered for publication in another journal.

That generative AI and AI-assisted technologies have not been utilized in the writing process or if used, disclosed in the manuscript the use of AI and AI-assisted technologies and a statement will appear in the published work.

That generative AI and AI-assisted technologies have not been used to create or alter images unless specifically used as part of the research design where such use must be described in a reproducible manner in the methods section.

All authors have been personally and actively involved in substantive work leading to the manuscript and will hold themselves jointly and individually responsible for its content.

Declaration of competing interest

The authors declare that they have no known competing financial interests or personal relationships that could have appeared to influence the work reported in this paper.

Acknowledgements

The authors thank the Instituto Nacional de Innovación Agraria (INIA) through the Investment Project with CUI N°. 2472675 entitled: “Mejoramiento de los servicios de investigación y transferencia de tecnología agraria en la estación agraria experimental Baños del Inca en la localidad de Baños del Inca del distrito de Baños del Inca - provincia de Cajamarca - departamento de Cajamarca” which funded the execution of this research.

ANNEX 1: Spectral variation in linear transects of three sections of system B

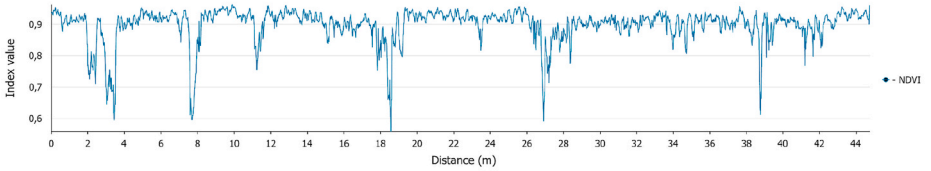
Index value
Distance (m)
- NDVI

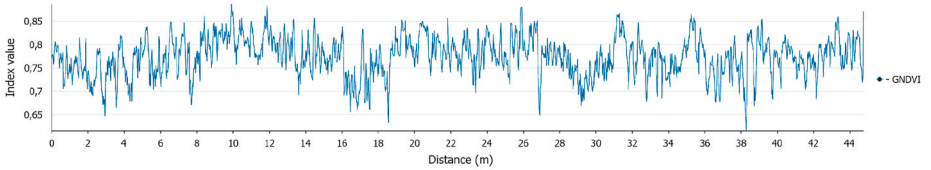
Index value
Distance (m)
- GNDVI

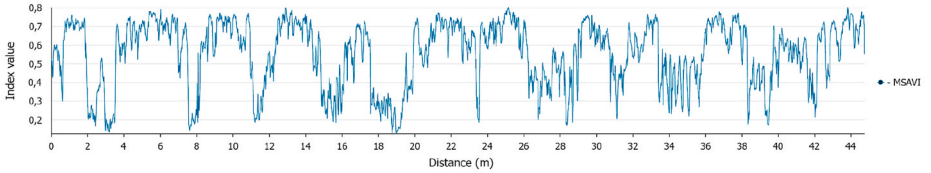
Index value
Distance (m)
- MSAVI

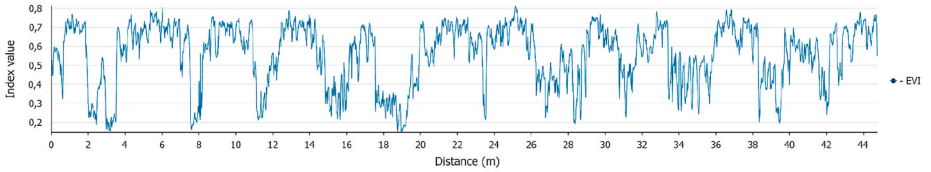
Index value
Distance (m)
- EVI

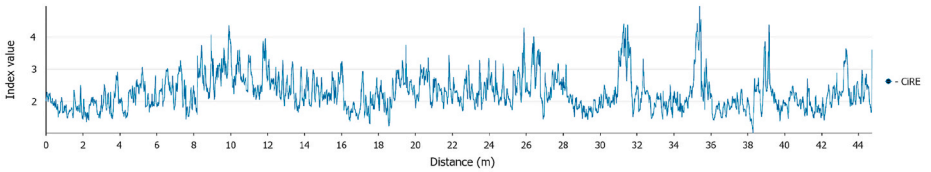
Index value
Distance (m)
- CIRE

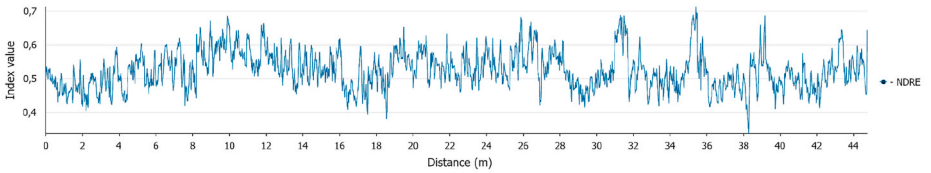
Index value
Distance (m)
- NDRE

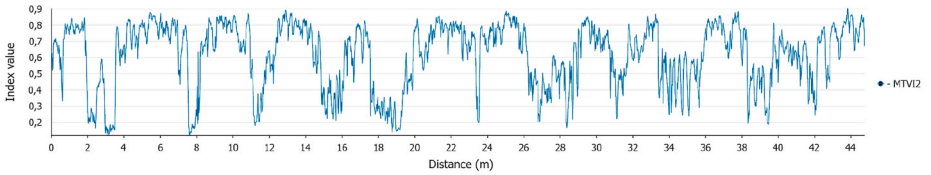
Index value
Distance (m)
- MTVI2

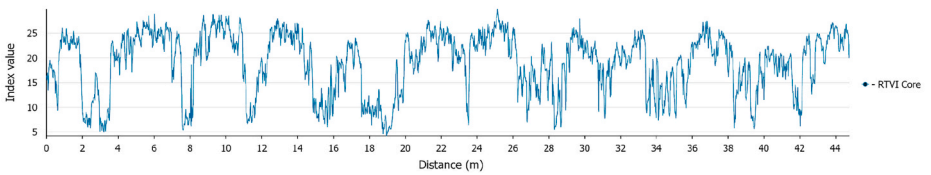
Index value
Distance (m)
- RTVI Core

Data availability

All supplementary material of this research can be found in the following repository: https://next.data.4tu.nl/private_datasets/6lRomsdQIElmnyF_3UZNOitrIm4rucmJHigdbfNy3MQ.

References

Anandita, K., Sinha, A.K., Jeganathan, C., 2024. Understanding and mitigating climate change impacts on ecosystem health and functionality. Rend. Lincei, Sci. Fis. Nat. 35, 793–818. https://doi.org/10.1007/S12210-024-01259-4.

Avtar, R., Suab, S.A., Syukur, M.S., Korom, A., Umarhadi, D.A., Yunus, A.P., 2020. Assessing the influence of UAV altitude on extracted biophysical parameters of young oil palm. Remote Sens. 12, 3030. https://doi.org/10.3390/RS12183030.

Brockerhoff, E.G., Barbaro, L., Castagneyrol, B., Forrester, D.I., Gardiner, B., González-Olabarria, J.R., Lyver, P.O.B., Meurisse, N., Oxbrough, A., Taki, H., Thompson, I.D., van der Plas, F., Jactel, H., 2017. Forest biodiversity, ecosystem functioning and the provision of ecosystem services. Biodivers. Conserv. 26, 3005–3035. https://doi.org/10.1007/S10531-017-1453-2.

Buschmann, C., Nagel, E., 1993. In vivo spectroscopy and internal optics of leaves as basis for remote sensing of vegetation. Int. J. Rem. Sens. 14, 711–722. https://doi.org/10.1080/01431169308904370.

Calders, K., Jonckheere, I., Nightingale, J., Vastaranta, M., 2020. Remote sensing technology applications in forestry and REDD+. Forests 11, 188. https://doi.org/10.3390/F11020188.

Chen, L., Ren, C., Bao, G., Zhang, B., Wang, Z., Liu, M., Man, W., Liu, J., 2022. Improved object-based estimation of forest aboveground biomass by integrating LiDAR data from GEDI and ICESat-2 with multi-sensor images in a heterogeneous mountainous region. Remote Sens. 14, 2743. https://doi.org/10.3390/RS14122743.

da Silva, S.D.P., de Paula Amaral, L., Aparecida Fantinel, R., Coelho Eugenio, F., 2024. RPAS-based forest plantation health monitoring: an overview of recent progress. Int. J. Rem. Sens. 45, 9131–9161. https://doi.org/10.1080/01431161.2024.2406036.

Dash, J.P., Pearse, G.D., Watt, M.S., 2018. UAV multispectral imagery can complement satellite data for monitoring forest health. Remote Sens. 10, 1216. https://doi.org/10.3390/RS10081216.

De Benedicto, S.C., Longo, R.M., Ferreira, D.H.L., Sugahara, C.R., Ribeiro, A.Í., Castañeda-Ayarza, J.A., Silva, L.H.V. da, 2025. Integrating strategies aimed at biodiversity and water resource sustainability in the amazonian region. Sustainability 17, 4010. https://doi.org/10.3390/SU17094010.

Dixit, J., Bhardwaj, A.K., Gupta, S.K., Singh, S.K., Meraj, G., Kumar, P., Kanga, S., Singh, S., Sajan, B., 2024. Potential of lightweight drones and object-oriented image segmentation in forest plantation assessment. Remote Sens. 16, 1554. https://doi.org/10.3390/RS16091554.

dos Reis, M., Graça, P.M.L. de A., Yanai, A.M., Ramos, C.J.P., Fearnside, P.M., 2021. Forest fires and deforestation in the central amazon: effects of landscape and climate on spatial and temporal dynamics. J. Environ. Manag. 288, 112310. https://doi.org/10.1016/J.JENVMAN.2021.112310.

Ecke, S., Dempewolf, J., Frey, J., Schwaller, A., Endres, E., Klemmt, H.J., Tiede, D., Seifert, T., 2022. UAV-based forest health monitoring: a systematic review. Remote Sens. 14, 3205. https://doi.org/10.3390/RS14133205.

Eugenio, F.C., Schons, C.T., Mallmann, C.L., Schuh, M.S., Fernandes, P., Badin, T.L., 2020. Remotely piloted aircraft systems and forests: a global state of the art and future challenges. Can. J. For. Res. 50, 705–716. https://doi.org/10.1139/CJFR-2019-0375.

Fao, Pnuma, 2020. El estado de los bosques del mundo 2020. Los Bosques, la Biodiversidad Y Las Personas. Roma.

Fassnacht, F.E., White, J.C., Wulder, M.A., Næsset, E., 2024. Remote sensing in forestry: current challenges, considerations and directions. Forestry: Int. J. Financ. Res. 97, 11–37. https://doi.org/10.1093/forestry/cpad024.

Gitelson, A.A., Merzlyak, M.N., 1998. Remote sensing of chlorophyll concentration in higher plant leaves. Adv. Space Res. 22, 689–692. https://doi.org/10.1016/S0273-1177(97)01133-2.

Gobierno Regional de Cajamarca (GRC), 2010. Zonificacion Ecologica Y Economica Como Base Para El Ordenamiento Territorial Del Departamento De Cajamarca.

Gu, Y.F., Jin, X.D., Xiang, R.Z., Wang, Q.W., Wang, C., Yang, S.X., 2020. UAV-based integrated multispectral-LiDAR imaging system and data processing. Sci. China Technol. Sci. 63, 1293–1301. https://doi.org/10.1007/S11431-019-1571-0/METRICS.

Haboudane, D., Miller, J.R., Pattey, E., Zarco-Tejada, P.J., Strachan, I.B., 2004. Hyperspectral vegetation indices and novel algorithms for predicting green LAI of crop canopies: modeling and validation in the context of precision agriculture. Remote Sens. Environ. 90, 337–352. https://doi.org/10.1016/J.RSE.2003.12.013.

Huete, A., Didan, K., Miura, T., Rodriguez, E.P., Gao, X., Ferreira, L.G., 2002. Overview of the radiometric and biophysical performance of the MODIS vegetation indices. Remote Sens. Environ. 83, 195–213. https://doi.org/10.1016/S0034-4257(02)00096-2.

Hyde, P., Dubayah, R., Walker, W., Blair, J.B., Hofton, M., Hunsaker, C., 2006. Mapping forest structure for wildlife habitat analysis using multi-sensor (LiDAR, SAR/InSAR, ETM+, quickbird) synergy. Remote Sens. Environ. 102, 63–73. https://doi.org/10.1016/J.RSE.2006.01.021.

Leitold, V., Keller, Michael, Morton, Douglas C., Cook, Bruce D., Shimabukuro, Yosio E., 2015. Airborne lidar-based estimates of tropical forest structure in complex terrain: opportunities and trade-offs for REDD+. Carbon Bal. Manag. 10, 1–12. https://doi.org/10.1186/S13021-015-0013-X.

Luo, W., Ma, Hongchao, Yuan, J., Zhang, L., Ma, Haichi, Cai, Z., Zhou, W., 2023. High-accuracy filtering of forest scenes based on full-waveform LiDAR data and hyperspectral images. Remote Sens. 15, 3499. https://doi.org/10.3390/RS15143499.

Maguya, A.S., Junttila, V., Kauranne, T., 2014. Algorithm for extracting digital terrain models under forest canopy from airborne LiDAR data. Remote Sens. 6, 6524–6548. https://doi.org/10.3390/RS6076524.

Morsdorf, F., Mårell, A., Koetz, B., Cassagne, N., Pimont, F., Rigolot, E., Allgöwer, B., 2010. Discrimination of vegetation strata in a multi-layered mediterranean forest ecosystem using height and intensity information derived from airborne laser scanning. Remote Sens. Environ. 114, 1403–1415. https://doi.org/10.1016/J.RSE.2010.01.023.

Móstiga, M., Armenteras, D., Vayreda, J., Retana, J., 2024. Two decades of accelerated deforestation in Peruvian forests: a national and regional analysis (2000–2020). Reg. Environ. Change 24, 1–12. https://doi.org/10.1007/S10113-024-02189-5/FIGURES/5.

Prevedello, J.A., Winck, G.R., Weber, M.M., Nichols, E., Sinervo, B., 2019. Impacts of forestation and deforestation on local temperature across the globe. PLoS One 14, e0213368. https://doi.org/10.1371/JOURNAL.PONE.0213368.

Qi, J., Chehbouni, A., Huete, A.R., Kerr, Y.H., Sorooshian, S., 1994. A modified soil adjusted vegetation index. Remote Sens. Environ. 48, 119–126. https://doi.org/10.1016/0034-4257(94)90134-1.

Ramírez, J.A., Marín, A., Urrego, J.B., Castaño, Á., Ospina, R., 2021. Efecto de la fertilización en el crecimiento de Retrophyllum rospigliosii de la zona andina colombiana. Madera Bosques 27. https://doi.org/10.21829/MYB.2021.2732315 e2732315–e2732315.

Rejeb, A., Abdollahi, A., Rejeb, K., Treiblmaier, H., 2022. Drones in agriculture: a review and bibliometric analysis. Comput. Electron. Agric. 198, 107017. https://doi.org/10.1016/J.COMPAG.2022.107017.

Restrepo, C., Alviar, M., 2010. Tasa de descuento y rotación forestal: el caso del Eucalyptus Saligna. Lect. Econ. 149–164.

Rouse, J.W., Hass, R.H., Schell, J.A., Deering, D.W., 1974. Monitoring Vegetation Systems in the Great Plains with ERTS, vol. 351. NASA Special Publication, p. 309.

Santoro, A., Venturi, M., Bertani, R., Agnoletti, M., 2020. A review of the role of forests and agroforestry systems in the FAO globally important agricultural heritage systems (GIAHS) programme. Forests 11. https://doi.org/10.3390/F11080860.

Seidel, D., Stiers, M., Ehbrecht, M., Werning, M., Annighöfer, P., 2021. On the structural complexity of central European agroforestry systems: a quantitative assessment using terrestrial laser scanning in single-scan mode. Agrofor. Syst. 95, 669–685. https://doi.org/10.1007/s10457-021-00620-y.

SENAMHI, 2020. Mapa climático del Perú [WWW Document]. URL. https://www.senamhi.gob.pe/?p=mapa-climatico-del-peru (accessed 10.21.20).

Sengupta, A., 2024. FOREST: future-oriented AI systems for enhancing plant health monitoring and sustainable treatments in precision agriculture. International Symposium on Technology and Society. https://doi.org/10.1109/ISTAS61960.2024.10732416.

Sims, D.A., Gamon, J.A., 2002. Relationships between leaf pigment content and spectral reflectance across a wide range of species, leaf structures and developmental stages. Remote Sens. Environ. 81, 337–354. https://doi.org/10.1016/S0034-4257(02)00010-X.

Song, H., Zhou, H., Wang, H., Ma, Y., Zhang, Q., Li, S., 2024. Retrieval of tree height percentiles over Rugged Mountain areas via target response waveform of satellite lidar. Remote Sens. 16, 425. https://doi.org/10.3390/RS16020425.

Stone, C., Mohammed, C., 2017. Application of remote sensing technologies for assessing planted forests damaged by insect pests and fungal pathogens: a review. Current Forestry Reports 3, 75–92. https://doi.org/10.1007/S40725-017-0056-1/METRICS.

Sun, Z., Zhong, R., Wu, Q., Guo, J., 2023. Airborne LiDAR strip adjustment method based on point clouds with planar neighborhoods. Remote Sens. 15, 5447. https://doi.org/10.3390/RS15235447.

Takhtkeshha, N., Mandlburger, G., Remondino, F., Hyyppä, J., 2024. Multispectral light detection and ranging technology and applications: a review. Sensors 24, 1669. https://doi.org/10.3390/S24051669.

Tan, H., Kou, W., Xu, W., Wang, L., Wang, H., Lu, N., 2025. Improved estimation of aboveground biomass in rubber plantations using deep learning on UAV multispectral imagery. Drones 9, 32. https://doi.org/10.3390/DRONES9010032.

Toth, C., Jóźków, G., 2016. Remote sensing platforms and sensors: a survey. ISPRS J. Photogrammetry Remote Sens. 115, 22–36. https://doi.org/10.1016/J.ISPRSJPRS.2015.10.004.

Wang, Y., Jia, X., Chai, G., Lei, L., Zhang, X., 2023. Improved estimation of aboveground biomass of regional coniferous forests integrating UAV-LiDAR strip data, Sentinel-1 and Sentinel-2 imageries. Plant Methods 19, 65. https://doi.org/10.1186/s13007-023-01043-9.

Warlo, H., Kautz, M., 2024. How do global forest pests respond to increasing temperatures? – a meta-analysis. Oikos 2024, e10842. https://doi.org/10.1111/OIK.10842.

Wu, L., Jiang, X., Peng, J., Wu, G., Xiong, X., 2023. A spectral preserved model based on spectral contribution and dependence with detail injection for pansharpening. Sci. Rep. 13, 6882. https://doi.org/10.1038/s41598-023-33574-5.

Yip, K.H.A., Liu, R., Wu, J., Hau, B.C.H., Lin, Y., Zhang, H., 2024. Community-based plant diversity monitoring of a dense-canopy and species-rich tropical forest using airborne LiDAR data. Ecol. Indic. 158, 111346. https://doi.org/10.1016/J.ECOLIND.2023.111346.

Yoshii, T., Matsumura, N., Lin, C., 2022. Integrating UAV-SfM and airborne lidar point cloud data to plantation forest feature extraction. Remote Sens. 14, 1713. https://doi.org/10.3390/RS14071713.

Zhang, D., Král, K., Krůček, M., Cushman, K.C., Kellner, J.R., 2024. Near-complete sampling of forest structure from high-density drone lidar demonstrated by ray tracing. Remote Sens. 16, 2774. https://doi.org/10.3390/RS16152774.

Zhao, J., Wang, J., Huang, J., Zhang, L., Tang, J., 2023. Spring temperature accumulation is a primary driver of forest disease and Pest occurrence in China in the context of climate change. Forests 14, 1730. https://doi.org/10.3390/F14091730.